J. Fluid Mech. (2013), *vol.* 718, *pp.* 5–38. © Cambridge University Press 2013
doi:10.1017/jfm.2012.579

Control of stationary cross-flow modes in a Mach 3.5 boundary layer using patterned passive and active roughness

Chan Yong Schuele, Thomas C. Corke† and Eric Matlis

University of Notre Dame, Institute for Flow Physics and Control, Aerospace and Mechanical Engineering Department, Notre Dame, IN 46556, USA

(Received 21 February 2012; revised 12 November 2012; accepted 20 November 2012; first published online 8 February 2013)

Spanwise-periodic roughness designed to excite selected wavelengths of stationary cross-flow modes was investigated in a three-dimensional boundary layer at Mach 3.5. The test model was a sharp-tipped 14° right-circular cone. The model and integrated sensor traversing system were placed in the Mach 3.5 supersonic low disturbance tunnel (SLDT) equipped with an axisymmetric 'quiet design' nozzle at NASA Langley Research Center. The model was oriented at a 4.2° angle of attack to produce a mean cross-flow velocity component in the boundary layer over the cone. The research examined both passive and active surface roughness. The passive roughness consisted of indentations (dimples) that were evenly spaced around the cone at an axial location that was just upstream of the first linear stability neutral growth branch for cross-flow modes. The active roughness consisted of an azimuthal array of micrometre-sized plasma actuators that were designed to produce the effect of passive surface bumps. Two azimuthal mode numbers of the passive and active patterned roughness were examined. One had an azimuthal mode number that was in the band of initially amplified stationary cross-flow modes. This was intended to represent a controlled baseline condition. The other azimuthal mode number was designed to suppress the growth of the initially amplified stationary cross-flow modes and thereby increase the transition Reynolds number. The results showed that the stationary cross-flow modes were receptive to both the passive and active patterned roughness. Only the passive roughness was investigated at a unit Reynolds number where transition would occur on the cone. Transition front measurements using the Preston tube approach indicated that the transition Reynolds number had increased by 35 % with the subcritical wavenumber roughness compared with the baseline smooth tip cone, and by 40 % compared with the critical wavenumber roughness. Based on the similarities in the response of the stationary cross-flow modes with the active roughness, we expect it would produce a similar transition delay.

Key words: boundary layers, boundary layer control, boundary layer stability

1. Introduction

Low-speed experiments by the group led by Saric & Reed (2002) have demonstrated that the application of micrometre-sized spanwise-periodic roughness can increase the

† Email address for correspondence: tcorke@nd.edu

https://doi.org/10.1017/jfm.2012.579 Published online by Cambridge University Press

transition to turbulence Reynolds number for boundary layer flows in which the cross-flow instability is the dominant mechanism. This is relevant to the wings of aircraft where large leading-edge sweep angles are used to minimize compressibility effects or maintain subsonic flow.

The first stage of cross-flow instability-dominated transition starts with the process of receptivity (Morkovin 1990*a*,*b*; Saric, Reed & Kerschen 2002; Reshotko 2008). Based on linear stability theory, travelling cross-flow modes are more amplified than stationary cross-flow modes. However, the stationary modes are highly receptive to surface roughness which can provide higher initial amplitudes that compensate for their lower amplification rate. As a result, except in instances of higher free stream turbulence levels (Bippes 1999), the stationary modes are the leading mechanism in cross-flow dominated transition.

As stationary cross-flow modes grow in amplitude, they form co-rotating vortices. As a result of their approximate alignment with the inviscid streamlines of the baseline flow, the vortices have a strong integrated effect on the boundary layer. As they reach larger amplitudes, they produce a mean flow distortion that includes the formation of an inflected mean velocity profile (Chernoray *et al.* 2005; White & Saric 2005). The inflectional velocity profile leads to a secondary inviscid instability that generates small-scale velocity fluctuations and eventually turbulence. These stages of development of the cross-flow instability are presented in comprehensive reviews by Reed & Saric (1989), Wasserman & Kloker (2002), Saric, Reed & White (2003) and Bonfigli & Kloker (2007).

The approach to control cross-flow instability-dominated transition to turbulence stems from the extreme receptivity of the instability to surface roughness. This feature was exploited by Corke & Knasiak (1998) and Corke, Matlis & Othman (2007) to excite selected wavenumbers of cross-flow modes in the boundary layer over a rotating disc, which is a canonical three-dimensional flow that exemplifies the cross-flow instability.

Saric, Ruben & Reibert (1998*b*) and Radeztsky, Reibert & Saric (1999) exploited this property in their swept wing experiments to excite fixed spanwise wavenumber stationary cross-flow modes using arrays of micrometre-sized circular distributed roughness elements. They demonstrated that stationary cross-flow modes at the forced spanwise wavenumber exclusively appeared in the boundary layer. Super-harmonic wavenumbers of the forced wavenumber were also possible to appear, however lower wavenumbers were always suppressed completely.

These observations led to the concept of exciting less amplified stationary cross-flow modes as a means of controlling transition to turbulent in these flows. The key element was that the spanwise wavenumber of the forced mode had to be higher than those of the naturally amplified band. This would guarantee that no disturbance energy would cascade through nonlinear interactions to lower, more-amplified wavenumbers. Saric *et al.* (1998*b*) referred to this approach of cross-flow transition control as ‘subcritical forcing’. This was in reference to the band of initially amplified spanwise wavenumbers being the ‘critical’ wavenumbers. Forcing of that amplified band of wavenumbers is then referred to as ‘critical forcing’.

Transition control comes by biasing the natural selection mechanism by raising the initial amplitude of the less-amplified cross-flow mode at the subcritical wavenumber, so that it initially dominates the instability growth process. The growth of the forced mode inhibits the growth of the more amplified (critical wavenumber) stationary mode by modifying the basic state. Ultimately the forced mode decays and the flow eventually becomes turbulent. However, in swept wing experiments (Saric *et al.* 1998*b*;

https://doi.org/10.1017/jfm.2012.579 Published online by Cambridge University Press

Radeztsky *et al.* 1999; Saric & Reed 2002), the approach has been shown to produce substantial increases in the transition Reynolds number.

Saric *et al.* (1998*b*) found that patterned surface roughness in the form of hemispherical 'dots' with a height of 50 μm, provided an effective transition delay in low-speed swept wing experiments. Reibert (1996) observed that for a fixed (subcritical) roughness spacing of $z = 12$ mm, the total disturbance amplitude grew to a constant saturation amplitude even when the roughness height was varied from 6 to 48 μm. Although the initial disturbance amplitude increased with larger roughness, the effects downstream relaxed and yielded similar looking mode shapes. In addition, Reibert (1996) documented that as the roughness height increased from 6 to 18 μm, in 6 μm increments obtained by stacking the roughness elements, transition occurred at the same location for all three roughness heights.

A majority of the experiments on cross-flow dominated transition to turbulence have been performed on swept wings at low, subsonic Mach number. However Saric & Reed (2002), Saric, Reed & Banks (2004), Semionov, Kosinov & Levchenko (2006) and Semionov & Kosinov (2007) have investigated the effect of distributed roughness on swept wings at supersonic Mach numbers.

Saric & Reed (2002) investigated a cooled swept wing in a wind tunnel experiment at Mach 2.4. The wing sweep angle was large enough to produce a subsonic leading edge. The patterned roughness they investigated included both raised bumps and depressions (dimples). Infrared thermographic images were used to indicate the onset of transition, which appeared as an increase in the wall temperature due to enhanced turbulent heat transfer. The experiments indicated that subcritical forcing would delay transition when compared with regions with critical forcing.

Saric *et al.* (2004) investigated subcritical forcing on a swept wing that was mounted under the fuselage of an F-15 aircraft. Infrared thermomography was again used to visualize the transition location. Although the patterned roughness was applied along a large portion of the wing span, transition was only found to be delayed near the wing tip. The authors speculated that the limited effect was due to flow interference from the fuselage of the aircraft.

Semionov *et al.* (2006) and Semionov & Kosinov (2007) conducted wind tunnel experiments on a 40° swept wing with 6 μm high distributed roughness at Mach 2.0. The transition location showed some sensitivity to the distributed roughness. However in contrast to the observations of Saric *et al.* (2003), the transition location was highly sensitive to the shape of the roughness. In further contrast, transition appeared to be slightly delayed with critical forcing rather than with subcritical forcing. More importantly, however, the measured mean flow distortion produced by the stationary cross-flow vortices did not match the roughness mode number. This suggests that there was a lack of receptivity to the roughness and that the results were for uncontrolled initial conditions.

Although a majority of cross-flow transition experiments have been on swept wings, a few have been conducted on right-circular cones at angles of attack. The conical flow at incidence generates a streamline-normal pressure gradient which, if properly designed, can lead to a mean cross-flow that is similar to that on a swept wing. Most relevant to the present study are the cone experiments by King (1992) at Mach 3.5, and by Wolf & Laub (1997) at Mach 1.6. Both of these studies were concerned with correlating transition data between wind tunnel and free-flight experiments. However, King (1992) was the first to mention the cross-flow instability as a transition mechanism.

https://doi.org/10.1017/jfm.2012.579 Published online by Cambridge University Press

In general, the cross-flow instability growth rate is a maximum where the cross-flow Reynolds number is a maximum. The cross-flow Reynolds number is defined as $Re_{CF} = V_{max}\delta/\nu$, where V_{max} is the maximum cross-flow velocity, normal to the edge inviscid streamline. For a cone at an angle of attack, the cross-flow Reynolds number increases and then decreases from the windward side of the cone to the leeward side. The maximum occurs towards an azimuthal location, θ, of $\sim$130°, where $\theta = 0°$ is the windward most ray on the cone, and $\theta = 180°$ is the leeward most ray.

Three different types of boundary layer instabilities are possible for a cone at an angle of attack. One is a Tollmien–Schlichting (TS) instability that occurs along the windward and leeward rays of the cone. The second is the cross-flow instability that will occur in the regions between the windward and leeward rays on the cone. Finally an inviscid inflectional instability can occur along the leeward ray of the cone. If the ratio of the cone angle of attack, α, and cone half-angle, ϕ_c, are properly chosen, the cross-flow instability will be the dominant boundary layer transition mechanism. King (1992) demonstrated that stationary cross-flow vortices were visible in the range $\alpha/\phi_c = 0.4$–0.8.

A majority of the previous cone models used in experiments have had highly polished surfaces. There are no experiments where patterned distributed roughness has been used on a cone at supersonic Mach numbers to control cross-flow-dominated transition.

A majority of the past research on periodic roughness used passive roughness ‘dots’ that were applied by hand. White & Saric (2000), however, examined an adaptive approach that used a flexible membrane stretched over holes in a wing section surface. The holes were connected to a manifold that could be pressurized to cause the membrane to balloon out causing half-spherical ‘bumps’ on the surface. The extension of the concept would have multiple manifolds connected to alternate holes that could be used to generate bumps of different spacing. To the best of the authors’ knowledge, this system was not developed further, however it points to the need for having this capability in a flight-ready transition-control system.

An alternate approach to providing the effect of spanwise-periodic roughness ‘bumps’ was developed by Corke (2001) and tested by Saric (W. S. Saric, Private communication, 2001) on a swept wing model (Saric *et al.* 1998*b*). It was based on a single dielectric barrier discharge plasma actuator design referred to as ‘plasma bumps’. The actuator consisted of ‘comb’ electrodes that overlapped a single bus electrode that was on the underside of a dielectric layer. Ionized air (plasma) was designed to form on the edges of the ‘comb’ electrodes in the regions were they overlapped the lower bus electrode. This resulted in a body force vector field (Corke, Enloe & Wilkinson 2010) that acted on the neutral airflow in the vicinity of each of the comb electrodes. The body force vector field was designed to cause the formation of counter-rotating vortices that were similar to that produced by a spanwise array of discrete surface roughness elements. The spacing of the ‘comb’ electrodes were designed to excite critical or subcritical wavenumbers of stationary cross-flow modes.

Given this background, the object of the present work was to investigate the receptivity of stationary cross-flow modes to patterned roughness at a supersonic free stream Mach number. Rather than a swept wing, the test model would be a sharp-tipped 14° right-circular cone at a 4.2° angle of attack. This would give $\alpha/\phi_c = 0.6$, which falls within the range where the cross-flow instability would be the dominant mechanism of transition. Both passive and active roughness would be investigated. These would each include critical and subcritical wavenumbers. The critical wavenumber roughness would represent a ‘controlled baseline’. The subcritical

https://doi.org/10.1017/jfm.2012.579 Published online by Cambridge University Press

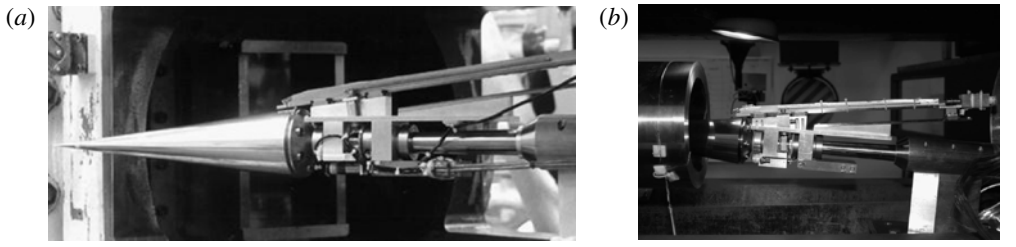


FIGURE 1. (*a*) Photograph of the cone model on the mounting sting with traversing mechanism outside the NASA Langley tunnel and (*b*) as viewed when mounted inside the Mach 3.5 axisymmetric nozzle.

wavenumber roughness would be designed to suppress the band of initially amplified stationary cross-flow modes and delay transition. The active roughness would be patterned after the 'plasma bumps' (Corke 2001). The choice of the wavenumbers and axial location of the patterned roughness would be guided by linear stability analysis of the basic flow over the cone. A polished smooth cone surface would be used to validate the linear theory predictions.

2. Experimental setup

The model used in the experiments was a hollow, thin-walled right-circular cone with a half angle of $\phi_c = 7°$. The model had been previously used by Corke, Cavalieri & Matlis (2002) and Matlis (2003). The total length of the cone is 35.56 cm (14 in). The first 4.303 cm (1.694 in) (tip) of the cone is removable.

The cone is made from 15-5ph stainless steel which was precipitation hardened to a H-1050 surface hardness, and polished to a mirror finish. The maximum downstream variation in the cone radius per centimetre is 0.002 mm (0.000079 in), which corresponds to approximately 1 % of the minimum boundary layer thickness based on the measurements by Matlis (2003). The model has 20 static pressure taps with a diameter of 0.76 mm (0.03 in) that are spaced 1.397 cm (0.55 in) apart and start 5.46 cm (2.15 in) downstream of the cone tip (Cavalieri 1995). A photograph of the circular cone outside of the wind tunnel is shown in figure 1(*a*).

The base of the cone is mounted to a hollow sting that is connected to a vertical strut. The vertical strut is bolted to a base plate that can be attached to the wind tunnel floor. Shims in the base plate were used to orient the cone at a mean angle of attack of $\alpha = 4.2°$. This gave $\alpha/\phi_c = 0.6$, which matched the largest dimensionless angle of attack examined by Stetson (1980), and was in the middle of the range of dimensionless angles where King (1992) documented stationary cross-flow vortices.

A motorized traversing mechanism mounted on the cone support sting moved a miniature total-pressure Pitot probe in the wall-normal, axial and azimuthal directions under computer control. Photographs of the traversing mechanism are shown in figure 2. Details of the traversing system are given by Schuele (2011). The motion resolution in the axial direction was 0.1 mm. The resolution in the azimuthal direction was 0.035°. This was 228 times smaller than the azimuthal wavelength of the initially amplified (critical) stationary cross-flow mode, and 160 times smaller than the azimuthal wavelength of the subcritical stationary cross-flow mode that was investigated for transition control. The resolution in the wall-normal direction

https://doi.org/10.1017/jfm.2012.579 Published online by Cambridge University Press

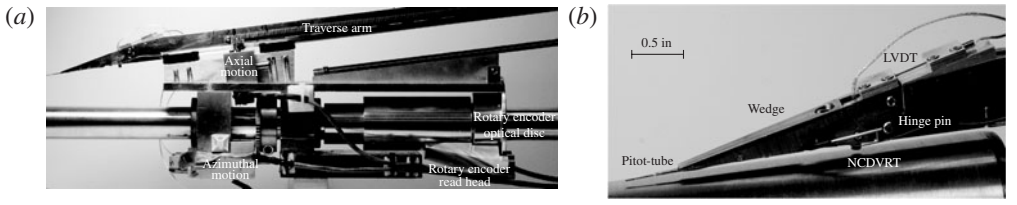


FIGURE 2. Photographs of (a) the traversing mechanism on the support sting without the cone (flow from left to right) and a zoomed-in view of the Pitot probe mounted on the tip of the traverse arm.

was 28 μm which was approximately 5 % of the boundary layer thickness based on previous measurements by Matlis (2003).

The Pitot probe design was a compromise between minimizing the flow interference, maximizing the spacial resolution and keeping the time constant for a pressure measurement as short as possible in consideration of the finite wind tunnel run times. The final design had an inner diameter of 0.25 mm, an outer diameter of 0.5 mm and was 12.5 mm long. This design allowed for good spatial resolution and minimum flow interference (Matlis 2003). The inner diameter corresponded to 17 % of the azimuthal wavelength of the initially amplified (critical) stationary cross-flow mode and 25 % of the azimuthal wavelength of the subcritical stationary cross-flow mode introduced in the experiment.

The Pitot probe pressure, static pressure ports on the cone and tunnel stagnation pressure were measured with Baratron 690 pressure transducers that used a MKS Type 670 signal conditioner. The transducer and signal conditioner had current calibrations to factory specifications of 0.08 % of the reading.

The data acquisition and traverse control was performed using a PMCCorp motion control card that included eight analogue-to-digital input channels. This was used to monitor the total pressure of the Pitot tube, the static pressure at the surface of the cone, a voltage indicating the contact made by the Pitot probe on the surface of the cone, the LVDT-Demodulator output indicating the wall-normal position of the Pitot probe and a voltage proportional to the temperature in the test section. This used custom software written specifically for the experiment.

The experiment was conducted in the Mach 3.5 supersonic low disturbance wind tunnel (SLDT) at the NASA Langley Research Center (Beckwith 1974; Wilkinson *et al.* 1992). The SLDT is a low-turbulence blow-down wind tunnel that can be operated at different stagnation pressures and temperatures. It uses a low-expansion axisymmetric nozzle that was designed to limit Görtler vortex formation. In addition, boundary layer suction slots near the nozzle throat remove the turbulent boundary layer that originates in the settling chamber and subsonic contraction. The combination of these features results in a constant Mach number 'quiet' test core. The streamwise extent of the test core depends on the total pressure, P_0, which determines the unit Reynolds number of the nozzle-wall boundary layers. Hot-wire measurements along the centreline of the nozzle at two stagnation pressures that bracket those used in the experiment, $P_0 = 172$ kPa (25 psi) and $P_0 = 345$ kPa (50 psi) and a total temperature of $T_0 = 311$ K (100.13 F), documented the extent of the quiet core to be 35.6 cm (14 in) and 27.9 cm (11 in), respectively (Kegerise, Owens & King 2010). At the lower stagnation pressure, the model was fully inside the 'quiet' test core. At the highest stagnation pressure, 79 % of the model was in the 'quiet' test core. Most

https://doi.org/10.1017/jfm.2012.579 Published online by Cambridge University Press

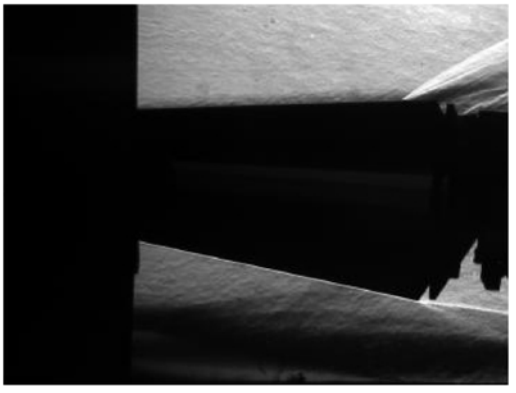


FIGURE 3. Schlieren flow visualization for a stagnation pressure of 172 kPa (25 psi) and a stagnation temperature of 311 K (100 F), where a majority of the measurements were performed.

importantly for the latter, the region of the linear instability development of the cone boundary layer was well inside the 'quiet' zone.

The experiment would typically run for 2–3 h in the NASA tunnel, which allowed the model to come to thermal equilibrium. This was accelerated because the portion of the model where the measurements were performed is thin skinned (Cavalieri 1995). Previous static temperature measurements by Matlis (2003) on the same cone for the same conditions confirmed adiabatic wall conditions.

Figure 3 shows Schlieren flow visualization that documents the condition with a stagnation pressure of 172 kPa (25 psi) and a stagnation temperature of 311 K (100 F, where a majority of the measurements were performed. It corresponds to a free stream unit Reynolds number of 9.8×10^6 m^{-1} (0.25×10^6 in^{-1}). The image shows that there are no shock waves impinging on the cone. The expansion waves observed at the base of the cone, at the upper right of the image, are due to the parked traverse mechanism. The boundary layer on the windward side (bottom) of the cone appears to be laminar, which is expected given the favourable pressure gradient that exists on that side of the cone. The boundary layer on the leeward side (top) of the cone is noticeably thicker than that on the windward side and appears to turbulent. Overall, the Schlieren image demonstrates that there were no unexpected disturbances present that might contaminate the boundary layer and cause transition to turbulence where it was not expected to occur.

2.1. *Patterned roughness*

The purpose of the subcritical patterned roughness was to excite stationary cross-flow modes that were outside of the initially amplified band of wavenumbers, but would amplify sufficiently to modify the mean flow and thereby suppress the more amplified cross-flow modes, delaying transition. The first step in the design of the experiment was to perform a linear stability analysis of the boundary layer flow over the cone for the experimental conditions. This was performed by Balakumar (2009). The basic flow simulation involved the solution of the compressible Navier–Stokes equations in cylindrical coordinates using a fifth-order accurate weighted essentially non-oscillatory (WENO) scheme for spatial discretization and using a third-order total-variation-diminishing (TVD) Runge–Kutta scheme for temporal integration. The linear

https://doi.org/10.1017/jfm.2012.579 Published online by Cambridge University Press

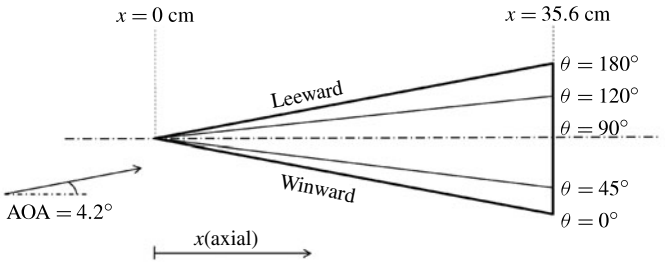


FIGURE 4. Schematic defining axial rays of constant azimuthal angle, θ, on the cone.

stability results were obtained from the local parallel theory at selected axial stations. N-factor traces were obtained from the emalik^{3d} code (Malik 1995). Each trace was obtained by starting the computations near the neutral point for a fixed frequency and marching downstream along the group velocity direction while seeking maximum growth rate at each station. N-factor computations performed by marching along the inviscid streamlines were found to yield almost the same traces and N-factor values.

The linear stability analysis predicted the location of the first neutral growth, Branch I, and the wavenumbers of the band of amplified stationary cross-flow modes. Growth rates, $-\alpha_i$, for the amplified stationary cross-flow modes along axial rays of constant azimuthal angles, θ, of 0, 45, 90 and 120°, as depicted in figure 4, are shown in figure 5. The growth rate curves of both stationary and travelling cross-flow modes are included in the figure. The notation F is the dimensionless frequency, where $F = 0$ are stationary modes, and m is the azimuthal wavenumber. The stationary mode growth curves have been highlighted with the square symbol. The horizontal (x) axis is the distance along the cone axis.

There are a number of important points to obtain from these results.

(i) The growth of cross-flow modes begins at approximately $x = 0.5$ in (1.27 cm). This means that the controlled disturbances (distributed roughness) have to be introduced at that location, or slightly upstream, so as not to compete with growing modes, which requires larger disturbance levels for control.

(ii) As expected, the growth rates of the travelling cross-flow modes are larger than those of the stationary modes. Therefore, the initial disturbance to the stationary modes has to be large enough to bias the outcome in favour of the stationary mode. The disturbances that feed the travelling mode are free stream turbulence and acoustics. Both of these have low levels in real flight conditions, as well as in the SLDT tunnel where the experiment was performed.

(iii) Finally, with respect to the azimuthal mode numbers for stationary modes, the initially amplified band is near $m = 50$.

Therefore, based on this analysis, we chose to examine three distributed roughness cases for the experiment:

(a) a baseline smooth cone surface;

(b) a controlled baseline of patterned roughness with an azimuthal mode number of $m = 45$ which is in the band of initially amplified stationary cross-flow modes; and

(c) a patterned roughness with a subcritical azimuthal mode number of $m = 68$ that is 1.5 times higher than the critical azimuthal mode number (Saric & Reed 2003).

https://doi.org/10.1017/jfm.2012.579 Published online by Cambridge University Press

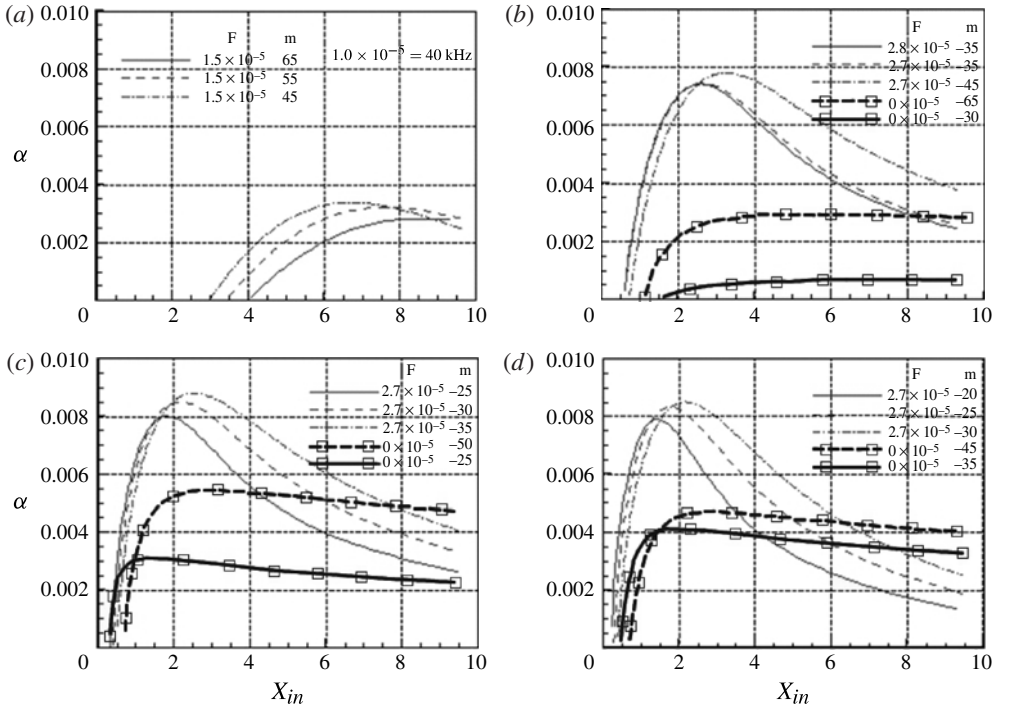


FIGURE 5. Growth rates along axial rays at constant azimuthal angles at $Re_\infty = 9.8\times10^6$ m^{-1} (0.25×10^6 in^{-1}): (*a*) $\theta = 0°$; (*b*) $\theta = 45°$; (*c*) $\theta = 90°$; (*d*) $\theta = 120°$. (From Balakumar (2009).)

The roughness was applied to different removable cone tips. The lower range of initially amplified azimuthal mode numbers ($m = 45$) for the controlled (critical) baseline condition was chosen because of the space constraints where they would be placed on the tip of the cone. This was particularly true for the subcritical patterned roughness with a 1.5 times higher mode number.

Both passive and active roughness were investigated. These are discussed in the two following subsections.

2.2. *Passive distributed roughness*

The passive roughness consisted of a smooth cone tip, and two cone tips with 45 or 68 indentations ('dimples') that were uniformly spaced around the circumference of the cone tip at 1.27 cm (0.5 in) from the tip of the cone. These cone tips were machined from Torlon, which is a relatively hard polymer that can be polished.

Historically, the type of patterned roughness used by others has been in the shape of spherical bumps (Saric *et al.* 1998*b*; Radeztsky *et al.* 1999). However, because of the small circumference (9.8 mm (0.386 in)) at the axial location on the cone tip where the patterned roughness was to be placed and the concern for achieving consistent bumps, we chose instead to use 'dimples'. In a private communication (W. S. Saric, Private communication, 2008), Saric indicated that both worked about the same.

The approach to produce the dimples was to use a pin with a conical end. The pin was plunged into the surface of the tip, with the depth determining the diameter of the hole at the surface. Control of the azimuthal spacing of the holes was done

https://doi.org/10.1017/jfm.2012.579 Published online by Cambridge University Press

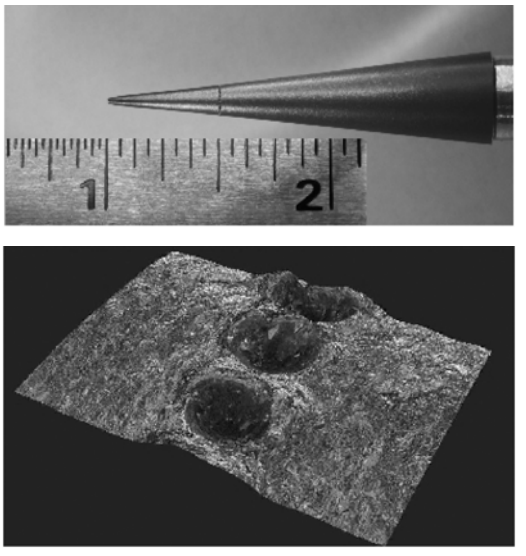


FIGURE 6. (*a*) Photograph of the cone tip with $m = 45$ dimples and (*b*) magnified view.

with a rotational indexing head on which the tip was mounted. Images of the $m = 45$ tip are shown in figure 6. Figure 6(*a*) shows a photograph of the removable cone tip with the $m = 45$ 'dimples' located 0.5 in from the point of the tip. Figure 6(*b*) is a magnified three-dimensional image that was acquired with a Keyence Model VHX-600 imaging microscope. A profile measurement indicated that the 'dimples' on the $m = 45$ tip were slightly oval, with an axial length of 180 μm and an azimuthal width of approximately 145 μm. The ratio of the diameter to azimuthal wavelength was then 0.65, which satisfied the requirement of Saric that $d/\lambda \geqslant 0.5$ (W. S. Saric, Private communication, 2008). The depth of the dimple holes was 39 μm. Finally, the three adjacent holes in the magnified image indicate that the size and shape of the 'dimples' was reasonably repeatable.

Images of the $m = 68$ tip are shown in figure 7. Figure 7(*a*) shows a photograph of the removable cone tip with the $m = 68$ 'dimples' located 0.5 in from the point of the tip. Figure 7(*b*) is a magnified three-dimensional image that was acquired with the imaging microscope. The smaller $m = 68$ wavelength allowed the holes to be smaller in diameter. As a result, the pin could be plunged to a smaller depth which resulted in round holes. The diameter of the $m = 68$ dimples was approximately 80 μm. This gave a diameter to azimuthal wavelength ratio of approximately 0.6. The magnified image indicates that the size and shape of the 'dimples' was very repeatable.

Our primary objective with the application of the patterned 'dimple' roughness was to make them as repeatable in shape as possible, and to satisfy the criteria (W. S. Saric, Private communication, 2008) that $d/\lambda \geqslant 0.5$. With regards to possible differences in initial amplitude between the $m = 45$ and $m = 68$ roughness arrays due to their different depths, we consider the analogy to arrays of roughness 'bumps'. As mentioned previously, Reibert (1996) documented that as the height of hemispherical bumps increased from 6 to 48 μm, the effects relaxed downstream and yielded similar looking mode shapes. In addition, Reibert (1996) documented that as the bump height increased from 6 to 18 μm, a factor of 3, the transition location remained the same. In our case, the ratio of the dimple depths for the two wavenumber roughness

https://doi.org/10.1017/jfm.2012.579 Published online by Cambridge University Press

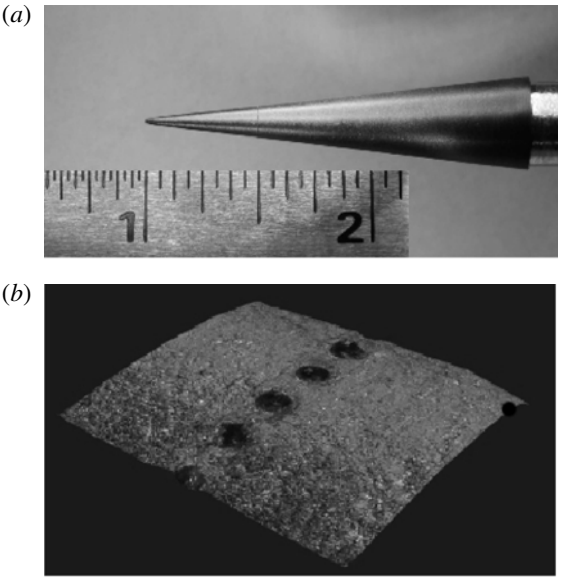


FIGURE 7. (*a*) Photograph of cone tip with $m = 68$ dimples and (*b*) magnified view.

was $de_{m=45}/de_{m=68} \simeq 1.8$, with the maximum depth of $de_{m=45} = 39$ μm. These placed the depth within the range where we expected a similar insensitivity with the dimple depth as Reibert observed with the bump heights.

2.3. *Active distributed roughness*

The active distributed roughness consisted of an azimuthal array of plasma actuators that had the same azimuthal wavenumbers as the passive roughness and were located at the same axial position on the removable cone tip. The plasma actuators were more specifically single dielectric barrier discharge (SDBD) plasma actuators that utilize two electrodes that are separated by a dielectric layer. One electrode is exposed to the air. The other electrode is covered by the dielectric layer. The SDBD plasma actuator electrically functions like a capacitor, and is therefore powered by an AC voltage source. When the AC voltage is large enough, the air near the exposed electrode weakly ionizes. The ionized air in the presence of the electric field produced by the electrode arrangement results in a body force vector field that acts on the neutrally charged air. An extensive review of SDBD plasma actuators was given by Corke *et al.* (2010).

The use of SDBD plasma actuators to produce the effect of distributed roughness for the control of stationary cross-flow modes was first examined by Corke (2001) and subsequently tested by Saric (W. S. Saric, Private communication, 2001). A photograph of a section of that plasma actuator array is shown in figure 8(*a*). The plasma actuator consisted of comb-like electrodes that overlapped a single bus electrode that was on the underside of a dielectric layer. The electrodes were vapour deposited onto a 0.8 mm thick glass-epoxy substrate. The comb electrodes were spaced 12 mm apart, which was the desired spanwise wavelength of stationary cross-flow modes to be excited. Ionized air (plasma) was designed to form on the edges of the comb electrodes in the regions were they overlap the lower covered electrode. This is illustrated in the schematic in the right part of figure 8. The body force vector field

https://doi.org/10.1017/jfm.2012.579 Published online by Cambridge University Press

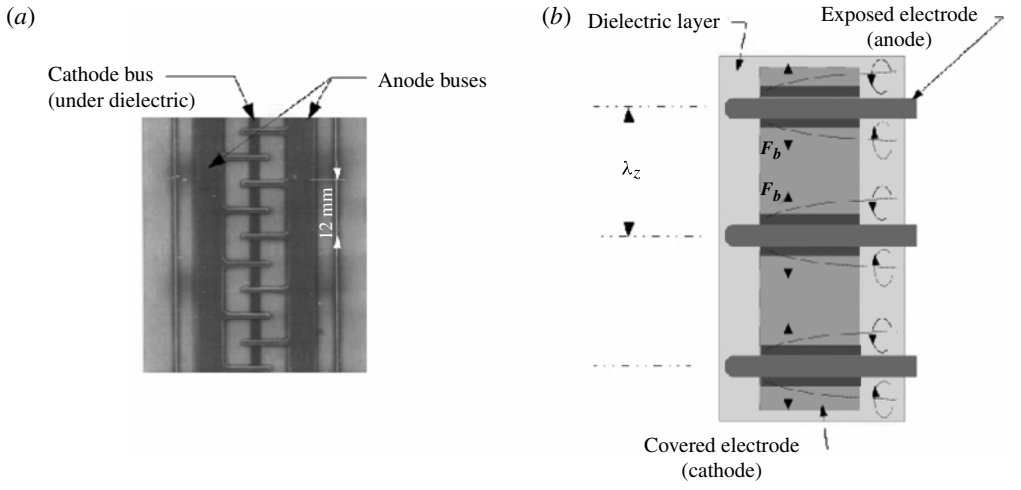


FIGURE 8. (*a*) Photograph of a section of the plasma actuator array developed by Corke (2001) and used by Saric (W. S. Saric, Private communication, 2001) in a demonstration of stationary cross-flow control and (*b*) schematic illustrating the body force vector field produced by the plasma actuator design.

is then perpendicular to the edges of the comb electrodes. This resulted in a spanwise velocity component.

In its application, the long axes of the comb electrodes was aligned with the mean flow direction. Therefore, the local spanwise flow field generated by each of the comb electrodes would result in a pair of counter-rotating streamwise vortices such as might be produced by the flow around an isolated wall protrusion (bump) (Morkovin 1990*a*,*b*).

The present experiment used the same basic design as that shown in figure 8. However, there were a number of significant challenges. The first was that the plasma actuator electrode array could not produce any passive roughness effect when not operated. This was also a requirement in the initial demonstration by Saric, however the thinner boundary layer thickness in the present experiment made this more of a challenge. The second challenge was the physical scale of the electrodes. For the $m = 68$ case, the centreline spacing between the electrodes would be 0.15 mm (0.0059 in), which is 80 times smaller than the array designed for Corke (2001) and Saric (W. S. Saric, Private communication, 2001). The final challenge was that the plasma actuator array needed to be applied on a curved, sloped surface which made fabrication more difficult.

A number of plasma actuator designs were investigated. These are presented in detail by Schuele (2011). The design that was used in the experiment is illustrated in figure 9. The removable cone tip consisted of two materials, a machinable ceramic (Macor) towards the tip and aluminum at the base. The Macor acts as the dielectric layer for the plasma actuator. The Macor part of the cone tip was drilled out to produce a lower section with a constant wall thickness of approximately 0.38–0.51 mm (15–20 mil). This resulted in a dielectric strength of 12–15 kVpp.

Conductive silver epoxy was used to fill the top of the tapered interior of the Macor part of the tip. This acted as the common covered electrode for the exposed electrodes. The silver epoxy also made the connection to the high-voltage (HV) wire lead that

https://doi.org/10.1017/jfm.2012.579 Published online by Cambridge University Press

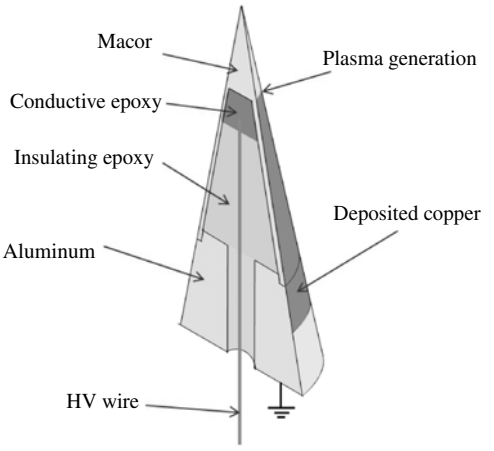


FIGURE 9. Schematic of the removable cone tip design for the plasma actuator array.

entered through the base of the removable cone tip. The wire was insulated by a fluorinated ethylene propylene (FEP) coating. It had an outer diameter of 1.27 mm (0.05 in) and a dielectric strength of 14 kVrms.

The tapered aluminum and Macor parts of the removable cone tip were bonded together with a fast curing non-conducting epoxy. The joined parts were then final machined to the precise conical shape and smoothed with 1800 grit sandpaper and a final lapping compound with an equivalent grit size of 3200.

The exposed electrode was made by depositing copper onto the outer surface of the cone tip, on top of the Macor and aluminum parts of the cone tip. In doing so, a continuous copper layer was electrically connected to the metal base of the cone tip, which when attached to the metal cone, was electrically grounded. The electrode 'comb' pattern was then etched into the exposed copper layer using photo-lithography techniques. The surface curvature of the cone tip was a big challenge for the photo-lithography. The details of the process are given by Schuele (2011).

The resulting 'comb' electrode structure is shown in figures 10 and 11. Figure 10(*a*) shows the overall view of the removable cone tip. The white portion of the tip is the unplated Macor. The bottom portion is the copper-plated portion of the tip. A magnified view of the edge of the copper plating obtained with the imaging microscope, is shown in figure 10(*b*). A more highly magnified view of the edge of the copper plating that clearly reveals the 'comb' electrode pattern is shown in figure 11. Both magnified views are for the smallest azimuthal wavelength, $m = 68$ case.

The dashed line in the magnified image in figure 11 denotes the edge of the covered electrode. The covered electrode is under the full length of the 'comb' electrodes and around the full azimuth of the tip, so that plasma will form between the electrodes like that shown in the illustration in figure 8.

The surface roughness of the plasma actuator cone tips was measured with a Zygo NewView 600 optical interferometer. Measurements of the copper-plated portion revealed an average plating thickness of 0.05 μm (0.197×10^{-6} in). In contrast, measurements on the unplated Macor portion of the cone tip documented the root mean square (r.m.s.) of the surface roughness to be 10 times larger than the plating

https://doi.org/10.1017/jfm.2012.579 Published online by Cambridge University Press

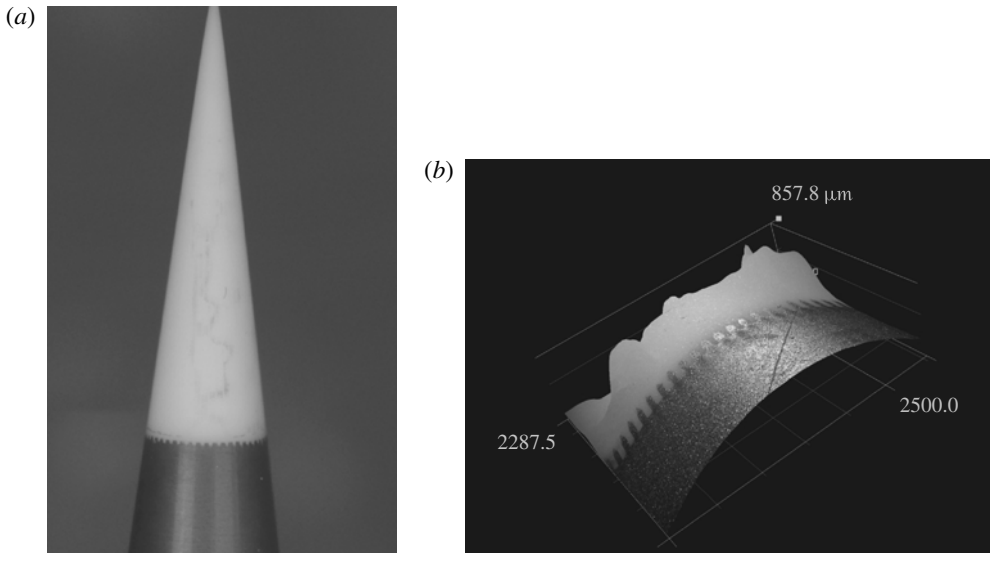


FIGURE 10. (*a*) Photograph of the plasma actuator cone tip and (*b*) magnified view of the edge of the copper plating showing the 'comb' electrode arrangement to excite $m = 68$ stationary cross-flow modes.

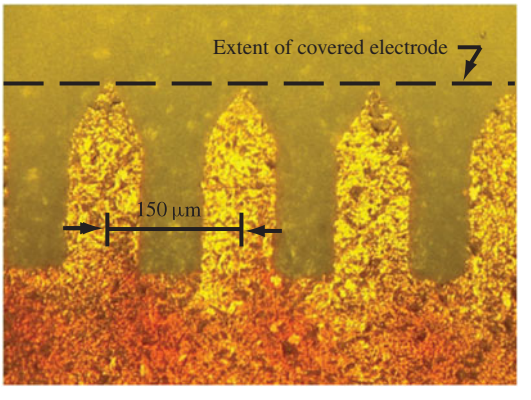


FIGURE 11. (Colour online) Largest magnification view of the edge of the copper plating showing the 'comb' electrode arrangement to excite $m = 68$ stationary cross-flow modes.

thickness. Therefore, the copper electrodes were indistinguishable from the passive roughness of the Macor cone tip surface.

Photographs of the plasma actuators on the cone tips when operating are shown in figure 12. These were operated in a pressure vessel in which the pressure was lowered to 10.2 kPa (3 inHg) to simulate the static pressure in the wind tunnel at Mach 3.5 and $P_0 = 172$ kPa. The AC input to the plasma actuator was a 5 kV_{p-p}, 5 kHz sine wave. The two left images are for the $m = 45$ cone tip. The right image is for the $m = 68$ cone tip. The top-left image is a side view of the $m = 45$ cone tip. The ionized air (plasma) is the blue illumination. All three images show azimuthally periodic illumination intensity that coincides with the locations of the exposed electrodes

https://doi.org/10.1017/jfm.2012.579 Published online by Cambridge University Press

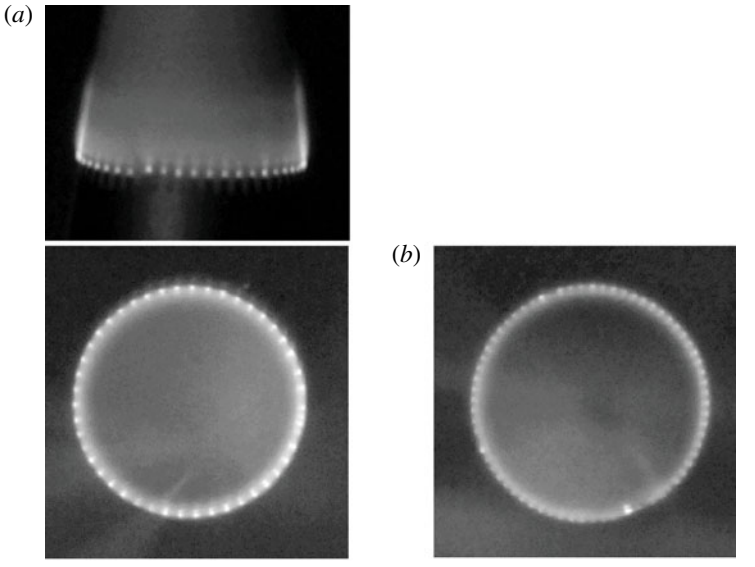


FIGURE 12. Long-time exposure of the plasma illumination pattern for the two plasma actuator cone tips designed to excite (*a*) $m = 45$ and (*b*) $m = 68$ stationary cross-flow modes. Top-left image is a side-view of the $m = 45$ cone tip.

around the cone tip. In addition, there is an axisymmetric plasma sheet that forms around the tip. This was not expected to have any effect on either the mean flow or the cross-flow instability.

3. Results: passive distributed roughness

These results document the receptivity of the stationary cross-flow mode to the passive patterned roughness with critical and subcritical azimuthal wavenumbers. Of themselves, these results are significant since they represent the first investigation of its type at high supersonic Mach numbers. The results with the passive roughness include surface flow visualization and azimuthal profiles of the total pressure at a fixed height in the boundary layer. Both measurements provide an indication of the presence and characteristics of the stationary cross-flow modes in the boundary layer with the three different roughness initial conditions.

3.1. *Surface flow visualization*

The surface flow visualization was intended to provide a global indication of the state of the stationary cross-flow modes for the different passive roughness cases. The approach was to apply to the surface of the cone a mixture of 15 parts 1000cSt silicon oil, 5 parts Oleic acid and 1 part titanium-dioxide powder. The left photograph in figure 13 shows the surface visualization oil before the wind tunnel was started. The right photograph in figure 13 records the pattern in the surface visualization oil after the wind tunnel had been operating for a sufficiently long amount of time whereby the oil pattern stopped changing. This was of the order of 4–5 min.

The long-time surface visualization image reveals light and dark bands. The presumption is that these bands result from the pumping action of the co-rotating stationary cross-flow vortices. The light bands correspond to an accumulation of the

https://doi.org/10.1017/jfm.2012.579 Published online by Cambridge University Press

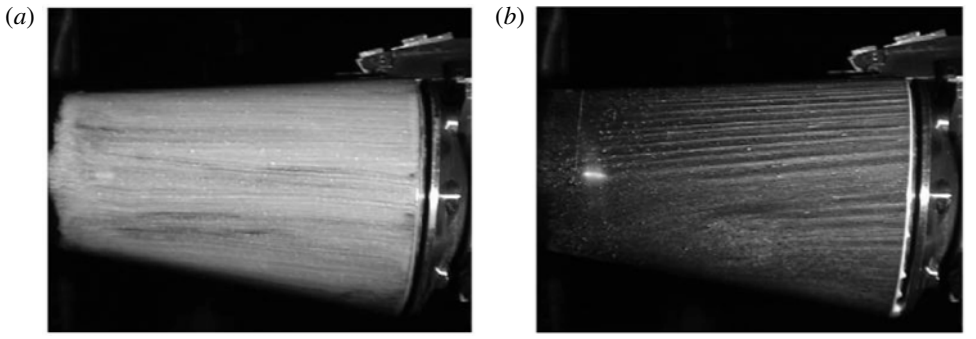


FIGURE 13. Photographs of (*a*) surface flow visualization as it appeared when initially applied and (*b*) after the pattern became stationary with the wind tunnel running. Conditions are for the baseline smooth cone tip at $P_0 = 172.4$ kPa (25 psi).

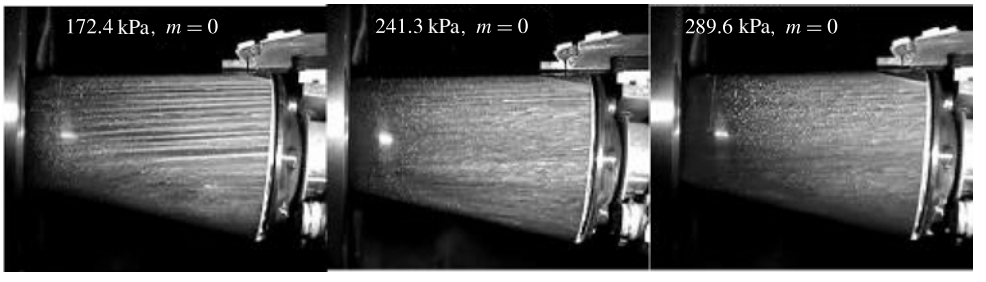


FIGURE 14. Photographs of surface flow visualization for the baseline smooth tip over a range of stagnation pressures that control the unit Reynolds number. Here $P_0 = 0172.4$ kPa (25 psi) is $Re = 9.84 \times 10^6$ m^{-1}, $P_0 = 241.3$ kPa (35 psi) is $Re = 1.37 \times 10^7$ m^{-1} and $P_0 = 289.6$ kPa (42 psi) is $Re = 1.65 \times 10^7$ m^{-1}.

surface marker (low shear stress) and the dark bands are where the surface marker has been depleted (high shear stress). Similar images have been observed with naphthalene surface visualization on swept wings by Saric & Reed (2003) and in surface oil visualization on cones at angles of attack by DiCrisitina (1970) and King (1992).

The condition shown in figure 13 corresponds to the baseline smooth tip at $P_0 = 172.4$ kPa (25 psi). Figure 14 shows a composite of the surface flow visualization for the smooth tip over a range of stagnation pressures (unit Reynolds numbers). The light and dark band pattern associated with the stationary cross-flow vortices is clearly visible at the lowest stagnation pressure (lowest unit Reynolds number). The linear stability analysis shown in figure 5 predicted that the maximum growth would occur along rays at constant azimuthal angles, θ, that were greater than 90°. This is consistent with the surface flow visualization in which coherent light–dark bands are not as evident at smaller (windward) azimuthal angles.

The organized band pattern is gradually lost as the stagnation pressure (unit Reynolds number) is increased. The speculation is that the boundary flow is becoming turbulent. The location of transition at the higher stagnation pressures will be estimated from the Pitot probe surveys.

Assuming that the light–dark bands in the surface flow visualization correspond to the presence of stationary cross-flow vortices, their spacing can be used for

https://doi.org/10.1017/jfm.2012.579 Published online by Cambridge University Press

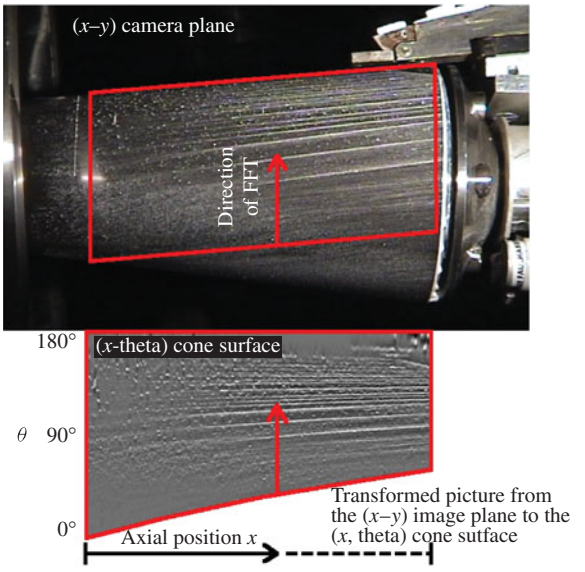


FIGURE 15. (Colour online) Sample result of the x–θ projection of a surface flow visualization image that was performed for image wavenumber analysis.

wavenumber analysis. To accomplish this, a coordinate transformation from the flat x–y camera plane onto a conical x–θ plane was performed. At a given axial location on the cone, the radius, $r(x)$, is known. Then the azimuthal angle, θ, was calculated from the observer plane at a distance, d, as $\theta = \sin^{-1}(d/r)$. With this, pixel coordinates were transformed into physical coordinates using known dimensions in the photographs. An example of a surface visualization conical-plane image is presented in figure 15, where the top image is the original photograph and the lower image is the projection onto the $x - \theta$ plane.

Following the conical-plane mapping of the images, a spectral analysis in the θ-direction was performed at each axial location in the surface flow visualization images. The resulting wavenumber spectrum maps are shown for the three passive roughness cases in figure 16. This shows surface flow visualization images with the corresponding wavenumber spectrum that was computed from the image. The left image and spectrum are for the baseline smooth tip ($m = 0$) condition. The middle image and spectrum are for the critical wavenumber, $m = 45$, roughness condition. The right image and spectrum are for the subcritical, $m = 68$, roughness condition. For all three, $P_0 = 172.4$ kPa (25 psi). The spectral amplitudes in each roughness case have been normalized by their respective maximum values. The normalized amplitudes range from zero, corresponding to the dark shading, to one, which corresponds to the light shading. The white horizontal lines mark azimuthal wavenumbers of interest.

In interpreting the spectral analysis of the flow visualization images, it is important to note that the analysis of the images includes all of the azimuthal extent that is visible. From the linear stability analysis in figure 5, the wavenumbers that are initially amplified depend on the azimuthal angle axial rays. For example at $\theta = 45°$ the largest growth is for $m = 65$, whereas for $\theta = 120°$ the largest growth is for $m = 50$. Therefore, the spectral analysis of the images that includes all of the azimuthal angles

https://doi.org/10.1017/jfm.2012.579 Published online by Cambridge University Press

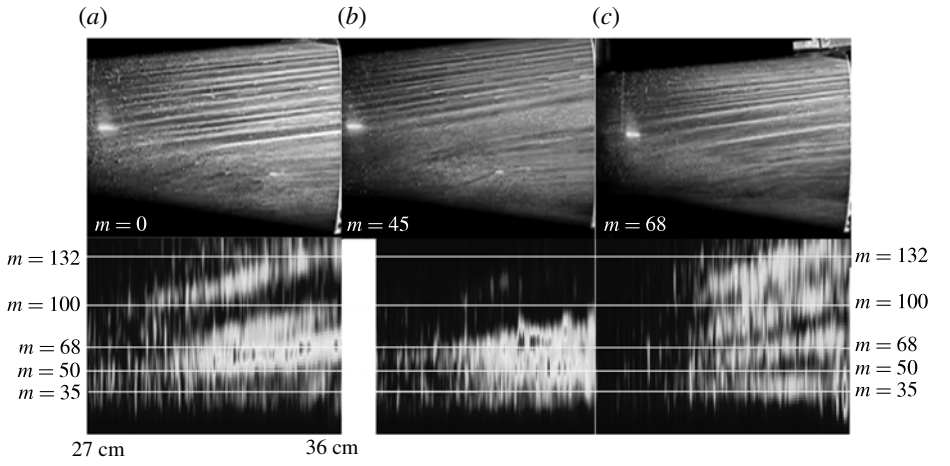


FIGURE 16. Photographs of surface flow visualization and corresponding wavenumber spectra for (*a*) the baseline smooth tip, (*b*) the $m = 45$ critical wavenumber roughness and (*c*) the $m = 68$ subcritical wavenumber roughness. Here $P_0 = 172.4$ kPa (25 psi) is $Re = 9.84 \times 10^6$ m^{-1}.

for the 'smooth' tip will be a composite of the different wavenumber stationary cross-flow modes that develop along these axial rays.

The wavenumber spectrum for the smooth tip shows that predominant azimuthal wavenumber (yellow band) at the most upstream location (27 cm) is $m \simeq 50$. This is among the first to amplify based on stability analysis (figure 5, $\theta = 120°$). The higher wavenumbers from smaller azimuthal angle rays (e.g. $\theta = 120°$) amplify further downstream and this leads to a gradual shift in the spectral band.

The wavenumber spectrum for the baseline smooth tip also exhibited significant energy at higher wavenumbers between $m = 100$ and $m = 130$. These might be the first harmonic of the critical stationary cross-flow mode that has been observed in experiments by Saric, Carrillo & Reibert (1998*a*).

The wavenumber spectrum for the critical wavenumber, $m = 45$, roughness is dramatically different from that of the baseline smooth tip. In particular, significant spectral energy now appears at lower wavenumbers between $m = 45$ and $m = 50$, especially at the furthest downstream location. In addition, the $m = 45$ roughness appears to have suppressed energy in the higher harmonic wavenumbers.

The wavenumber spectrum for the subcritical wavenumber roughness clearly indicates spectral energy at the target $m = 68$ wavenumber. In addition, it appears to have suppressed energy in the initially amplified range between $m = 50$ and $m = 60$. In contrast to the critical wavenumber roughness, energy at higher wavenumbers is present, somewhat like with the smooth cone tip.

3.2. *Pitot probe measurements*

Pitot probe surveys provided a direct measure of the mean flow distortion in the boundary layer, to complement results from the surface flow visualization. The surveys involved measurements at discrete azimuthal locations at a constant height above the cone surface, inside the boundary layer. The Pitot probe measured the variation in the time-averaged total pressure, P_t that provided an indication of the mean thickening

https://doi.org/10.1017/jfm.2012.579 Published online by Cambridge University Press

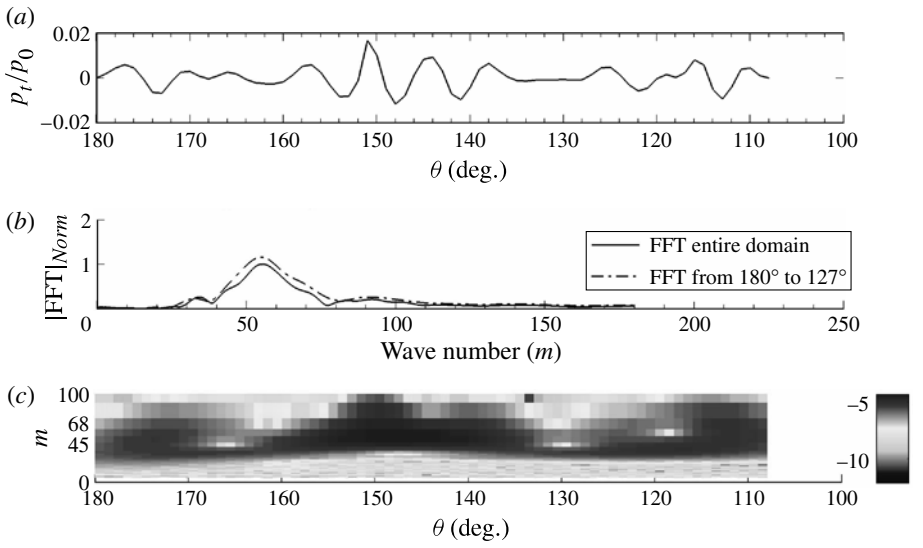


FIGURE 17. Azimuthal variation in mean pressure in the boundary layer at $x = 28.45$ cm ($Re_x = 2.79 \times 10^6$) for (*a*) the baseline smooth tip $m = 0$ (normalized pitot probe measurements), and (*b*) corresponding wavenumber spectra of the pressure variation (amplitude spectrum of the normalized pitot total pressure) and (*c*) wavelet analysis (log amplitude scale of the normalized pitot pressure).

and thinning of the boundary layer in the azimuthal direction. In these plots, P_t was normalized by the stagnation pressure, P_0.

The azimuthal variation of the total pressure in the boundary layer for the smooth baseline ($m = 0$) tip is shown in figure 17. This corresponds to an axial location of $x = 28.45$ cm (11.2 in), which for $P_0 = 172.4$ kPa (25 psi) corresponds to $Re_x = 2.79 \times 10^6$. This location is close to the upstream edge of the flow visualization image for the smooth tip in figure 16. The top plot in the figure corresponds to the normalized azimuthal pressure distribution. The middle plot corresponds to the amplitude spectrum of the azimuthal pressure distribution. The solid curve is the spectrum for the whole azimuthal domain. The dashed curve is the spectrum for $127^\circ \leqslant \theta \leqslant 180^\circ$. The bottom plot is a wavelet analysis of the azimuthal pressure distribution. This indicates the azimuthal distribution of energy in azimuthal mode numbers.

The spectrum of the azimuthal mean pressure variation in figure 17 indicates energy in wavenumbers that is consistent with the wavenumber analysis of the surface flow visualization. This indicates an energetic band between $40 \leqslant m \leqslant 70$, that is consistent with the linear theory predictions. The largest energy is at $m \simeq 55$. We also note that there was very little difference between the spectra when considering the whole domain or part of the azimuthal domain for the smooth tip.

The $m = 45$ roughness was intended to be a 'controlled baseline'. As such, it was designed to excite stationary cross-flow modes in the initially amplified band of wavenumbers. The wavenumber spectra in figure 18(*b*) confirm this, with the dominant peak occurring at $m = 45$ when the entire azimuthal domain is included. However, in contrast to the smooth tip, the spectra with the $m = 45$ roughness tip depend on

https://doi.org/10.1017/jfm.2012.579 Published online by Cambridge University Press

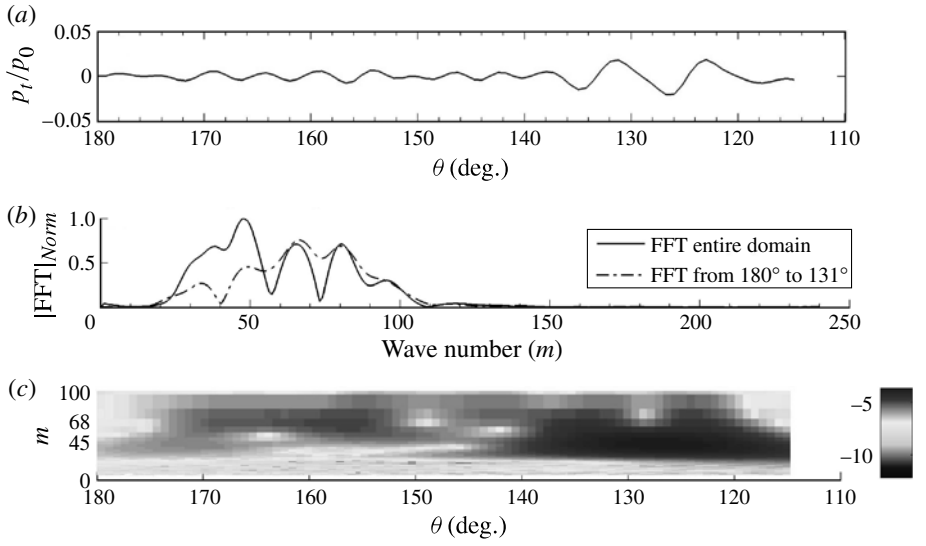


FIGURE 18. Azimuthal variation in mean pressure in the boundary layer at $x = 28.45$ cm ($Re_x = 2.79 \times 10^6$) for (*a*) the $m = 45$ roughness (normalized pitot probe measurements), and (*b*) corresponding wavenumber spectra of the pressure variation (amplitude spectrum of the normalized pitot total pressure) and (*c*) wavelet analysis (log amplitude scale of the normalized pitot pressure).

the azimuthal extent of the measurement. This observation leads to our concept of a 'dividing line' that will be discussed in a portion of the paper to follow.

The $m = 68$ roughness was intended to suppress energy in the initially amplified band of wavenumbers by putting energy into a higher less-amplified band. Examining the wavenumber spectra in figure 19 appears to give a mixed view on its success. If the entire azimuthal domain is taken, the spectrum is not that much different than that of the smooth tip, baseline condition. However, if a smaller azimuthal extent on the leeward portion of the cone is analysed, it is clear that the energy has shifted to the higher wavenumbers with the addition of the $m = 68$ roughness.

The wavenumber spectra and wavelet analysis indicated that both of the patterned roughnesses located near the tip of the cone influenced only a portion of the azimuthal extent of the cone. Therefore, in evaluating the receptivity of the stationary cross-flow modes to the roughness, it was first necessary to determine the reason for the apparent azimuthal sensitivity. For this, we concentrated on the subcritical $m = 68$ roughness.

The azimuthal distribution of the total pressure at a fixed height in the boundary layer at different axial locations was measured for the $m = 68$ roughness. These are shown in figure 20. The paths of the stationary cross-flow vortices were identified by connecting the pressure maxima in the azimuthal distributions. These are shown as dashed curves.

The cross-flow vortex trajectories in figure 20 were overlaid onto a plot of the mean surface streamlines of the basic flow for the cone at the 4.2° angle of attack. This is shown in figure 21. Also included in the figure are the predicted paths of $m = 40$ stationary cross-flow vortices based on a DNS simulation by Balakumar (2009).

The top part of figure 21 shows the data in x–θ coordinates. The bottom part of the figure shows the same data projected on the physical surface of the cone.

https://doi.org/10.1017/jfm.2012.579 Published online by Cambridge University Press

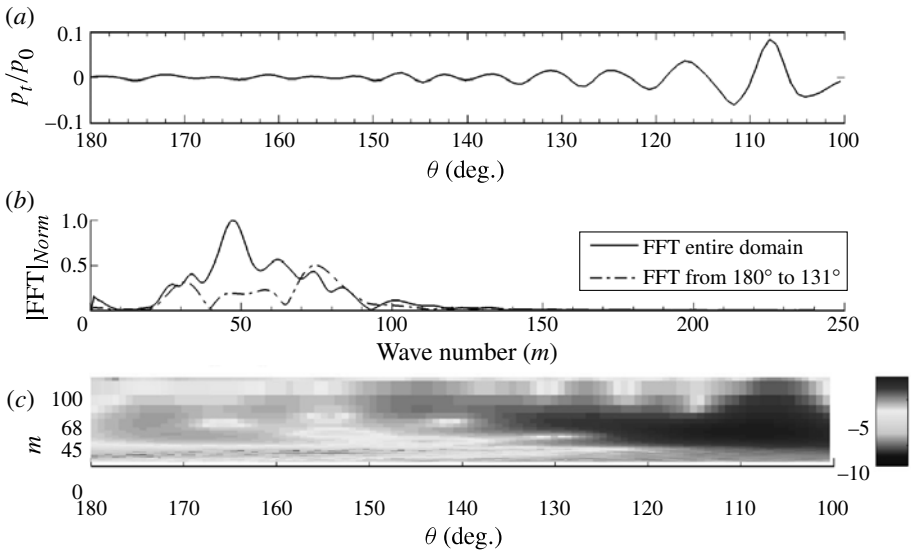


FIGURE 19. Azimuthal variation in mean pressure in the boundary layer at $x = 28.45$ cm ($Re_x = 2.79 \times 10^6$) for (*a*) the $m = 68$ roughness (normalized pitot probe measurements), and (*b*) corresponding wavenumber spectra of the pressure variation (amplitude spectrum of the normalized pitot total pressure) and (*c*) wavelet analysis (log amplitude scale of the normalized pitot pressure).

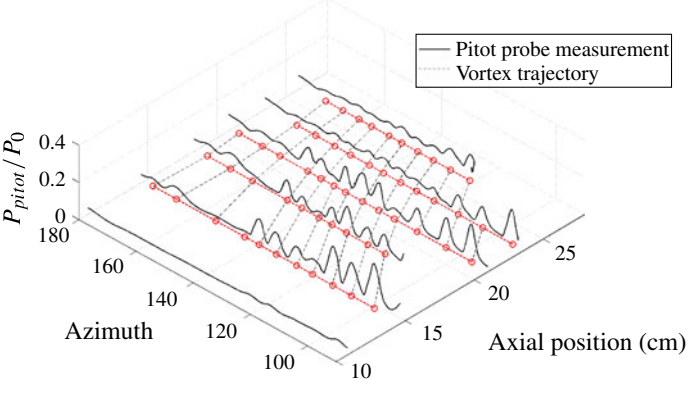


FIGURE 20. (Colour online) Azimuthal variation in mean pressure in the boundary layer for the $m = 68$ roughness at different streamwise locations with $P_0 = 172.4$ kPa (25 psi).

Even though the wavenumbers of the cross-flow modes are different between the experiment and simulation, the vortex trajectories agree fairly well. This suggests that the simulated vortex paths could be used to predict the paths of the measured cross-flow vortices into regions where measurements were not taken. This is particularly important for extrapolating in the upstream direction towards the location of the distributed roughness array at $x = 1.27$ cm (0.5 in). Based on this, we note that most of the paths of cross-flow vortices originated near the windward side of the cone. This is not surprising since the stationary cross-flow modes are expected to generally follow

https://doi.org/10.1017/jfm.2012.579 Published online by Cambridge University Press

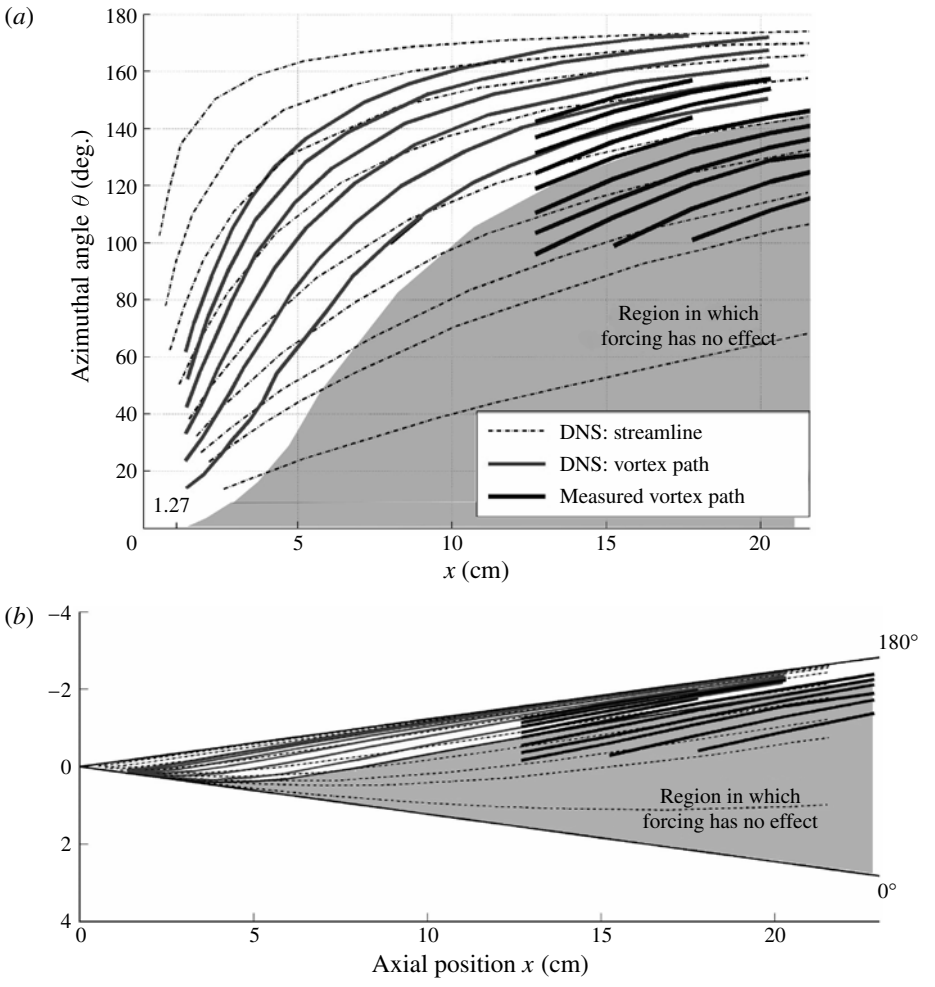


FIGURE 21. Measured stationary cross-flow vortex paths for $m = 68$ roughness along with paths of surface streamlines of the basic flow and the $m = 40$ cross-flow modes based on DNS simulation of Balakumar (2009): (*a*) *x*-theta plane; (*b*) *x*–*y* projection. Here $P_0 = 172.4$ kPa (25 psi).

the mean flow streamlines, and they originate on the windward side of the cone. The result suggests that there is an azimuthal 'dividing line' below which the roughness placed near the tip of the cone would have no effect. This region below the dividing line has been shaded in grey. Therefore, judgment on the effectiveness of the patterned roughness should only be applied to the region above the dividing line, which is not shaded.

This conclusion was further verified by wavenumber spectral analysis of the azimuthal pressure distributions at three of the axial locations in figure 20 in the range of $1.25 \times 10^6 \leqslant Re_x \leqslant 1.75 \times 10^6$. This is shown in figure 22. The rows in the figure correspond to the three axial Reynolds numbers, increasing from bottom to top. The left column shows the azimuthal pressure distributions. The horizontal bar above the pressure distributions defines two regions, (a) and (b). The interface between

https://doi.org/10.1017/jfm.2012.579 Published online by Cambridge University Press

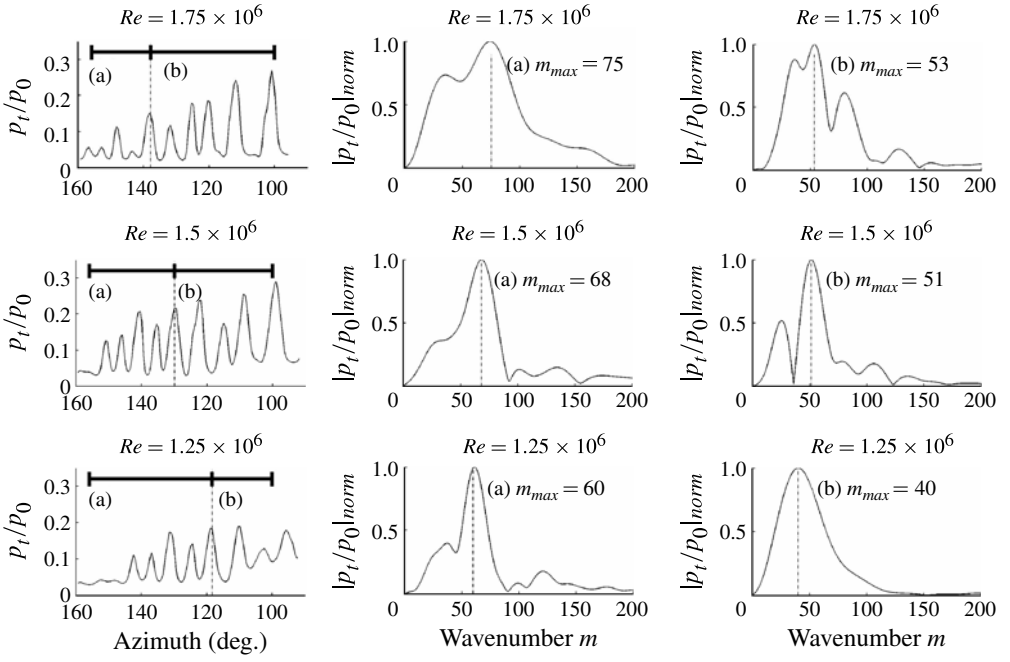


FIGURE 22. Comparison of wavenumber spectra of stationary cross-flow modes with the $m = 68$ roughness tip when sampled on either side of the 'dividing line' defined in figure 21. Here $P_0 = 172.4$ kPa (25 psi).

regions (a) and (b) is the azimuthal location of the 'dividing line' at the respective axial locations based on figure 21. Region (a) corresponds to the leeward side of the dividing line where the roughness should be effective. Region (b) corresponds to the windward side of the dividing line where the roughness should not be effective.

In region (a), the spectra indicate significant energy near $m = 68$. In contrast in region (b), the spectra indicate significant energy near $m = 50$, which is in the amplified band of stationary cross-flow modes from the linear stability analysis. This indicates that in region (b) which is on the windward side of the dividing line, the mean flow does not encounter the $m = 68$ patterned roughness at the cone tip and develops as if the cone tip were smooth.

Having now defined the azimuthal region where the effect of the patterned roughness can be evaluated, an experiment was performed to verify the repeatability of the measurements. The result of this is shown in figure 23. This shows azimuthal distributions of the total pressure at a fixed height in the boundary layer at one axial location ($x = 25.9$ cm) at $P_0 = 172.4$ kPa (25 psi). The left plot shows successive measurements for the smooth cone tip. The right plot shows similar successive measurements for the $m = 68$ roughness tip. For the successive measurements, the wind tunnel was stopped and restarted. For the smooth tip, the amplitude and locations of the peaks and valleys, signifying the locations and strength of the stationary cross-flow vortices, varies somewhat from run to run. We suspect that these differences were due to minute particles that settled on the cone tip during or between runs. In contrast, the azimuthal pressure distributions are very precisely repeatable on the leeward side of the dividing streamline at this axial location, $\theta \geqslant 130°$.

https://doi.org/10.1017/jfm.2012.579 Published online by Cambridge University Press

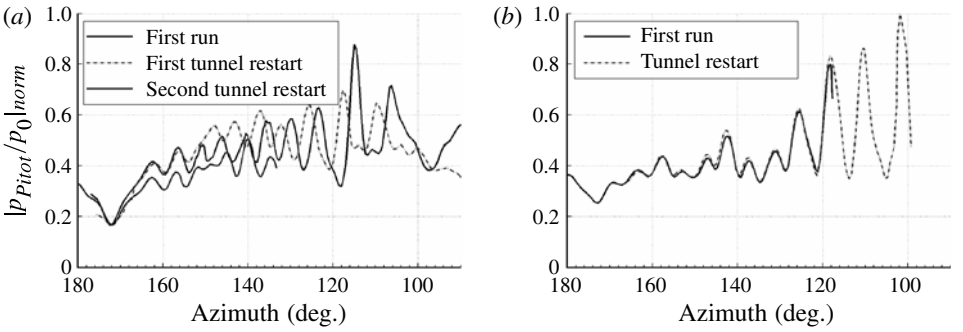


FIGURE 23. Repeated azimuthal profiles of the total pressure at a fixed height in the boundary layer following the wind tunnel being started and stopped, for (*a*) the smooth cone tip and (*b*) the $m = 68$ roughness cone tip. Here $P_0 = 172.4$ kPa (25 psi) with: (*a*) $x = 25.9$ cm, $m = 0$ (smooth cone tip); (*b*) $x = 25.9$ cm, $m = 68$ (dimple cone tip).

3.2.1. *Transition front detection*

The original motivation for the use of patterned roughness with subcritical wavenumbers has been to increase transition Reynolds numbers. Therefore, this aspect was investigated in the present experiment. This required increasing the stagnation pressure (unit Reynolds number) in the experiments so that natural transition would occur in the measurable region on the cone. Based on surface flow visualization such as shown in figure 14, a stagnation pressure of $P_0 = 310.3$ kPa (45 psi) was chosen. This gave a unit Reynolds number of $Re = 1.77 \times 10^7$ m^{-1}.

The measurements consisted of azimuthal profiles of the total pressure at a fixed height in the boundary layer for different axial locations. This was performed for both the $m = 45$ and $m = 68$ patterned roughness. The resulting measurements are shown in figure 24. The format of the figure is similar to that of figure 20, except the azimuthal extent is smaller, and the discrete points were interpolated to form a more continuous sheet in the $Re_x - \theta$ plane. Greyscale rendering was added to better highlight the peaks and valleys in the pressure distribution, as well as their axial development.

It appears obvious from figure 24 that the coherent azimuthal pressure fluctuations that we associate with the boundary layer mean flow distortion decay faster with the $m = 45$ roughness than with the $m = 68$ roughness. In order to quantify this, the r.m.s. of the pressure variation in the azimuthal direction was calculated at each axial location. The result is presented in figure 25. This confirms that the coherent mean flow distortion associated with the stationary cross-flow vortices decays in the axial direction much more quickly with the critical $m = 45$ roughness than with the subcritical $m = 68$ roughness. Saric *et al.* (1998*b*) and Saric & Reed (2003) proposed that the loss of the coherent mean flow distortion was an indication of transition in cross-flow dominated flows. We might conclude that this criterion indicates the end of transition. Based on this interpretation, transition that occurred at $Re_x \simeq 2.5 \times 10^6$ with the critical wavenumber forcing, was delayed to $Re_x \simeq 3.5 \times 10^6$ with subcritical wavenumber forcing.

A second estimate for the transition location used a Preston tube approach. This approach had been used by King (1992) in a similar experiment on a cone at an angle of attack at Mach 3.5. However, in that experiment, patterned roughness was not used so that it would be unlikely that the stationary cross-flow modes were as spatially correlated as in the present experiment. In the present experiment, the Preston tube

https://doi.org/10.1017/jfm.2012.579 Published online by Cambridge University Press

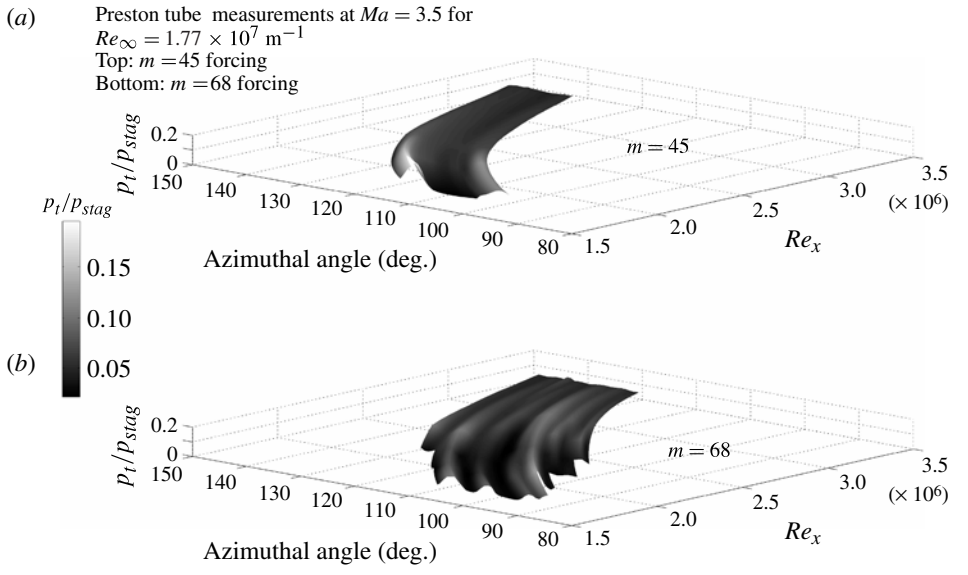


FIGURE 24. Azimuthal variation in mean pressure in the boundary layer for the (*a*) $m = 45$ and (*b*) $m = 68$ roughness at different streamwise locations with $P_0 = 310.3$ kPa (45 psi).

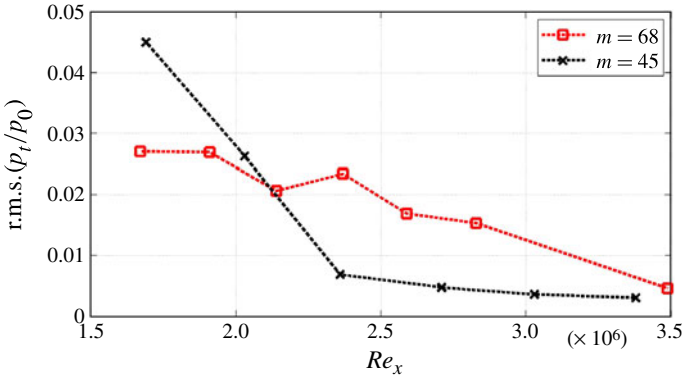


FIGURE 25. (Colour online) Axial development of the r.m.s. of the mean pressure variation in the azimuthal direction for the critical and subcritical patterned roughness.

approach was the only method used to detect the transition front for the uncontrolled baseline, smooth tip case.

The basis for transition detection using a Preston tube is the occurrence of a large increase in the total pressure near the wall that signifies an increase in the wall shear. We might conclude that this criterion indicates the beginning of transition. The challenge with this technique with the patterned roughness is in distinguishing between an increase in the wall shear produced by transition, and that associated with the mean flow distortion produced by the spatially correlated cross-flow vortices.

In order to overcome this issue, the streamwise change in the total pressure at the cone surface was measured along a path that was parallel to the path of the

https://doi.org/10.1017/jfm.2012.579 Published online by Cambridge University Press

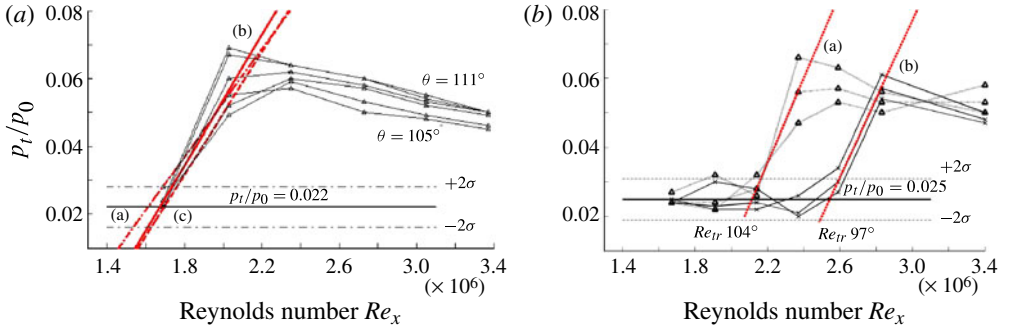


FIGURE 26. (Colour online) Axial development of the normalized total pressure between a pair of stationary cross-flow vortices for the (*a*) critical and (*b*) subcritical patterned roughness: (*a*) $m = 45$ pressure traces along vortex coordinates of the low-pressure region; (*b*) $m = 68$ pressure traces along vortex coordinates of the low-pressure region.

stationary cross-flow vortices. More specifically, the measurement was performed in the minimum pressure region between a pair of stationary cross-flow vortices. The axial pressure distributions that resulted are shown in figure 26.

Figure 26 shows the normalized total pressure at the wall as a function of the local Reynolds number, Re_x, that was based on the axial position. The left plot corresponds to the critical ($m = 45$) patterned roughness. The right plot is for the subcritical ($m = 68$) roughness. For the $m = 45$ roughness, the different data curves correspond to measurements taken at different azimuthal locations in 1° increments around the pressure minimum between the pair of cross-flow vortices. These indicate a rapid increase in the pressure at the wall followed by slow decrease that are characteristic of a Preston tube measurement of boundary layer transition (King 1992). Linear least-squares-error fits were applied to the rapid increasing portion of the pressure data. The start of transition was designated to be the Reynolds number at which the linear curves intercepted an average, pretransitional, pressure baseline. The baseline was chosen as $P_t/P_0 = 0.022$. This is indicated by the solid horizontal line. The two horizontal dash-dotted lines indicate a 95 % confidence interval on the pressure baseline. Based on this, the transition Reynolds number was determined to be $1.61 \times 10^6 \leqslant Re_{x_{trans}} \leqslant 1.71 \times 10^6$. The range of $Re_{x_{trans}}$ are denoted as (a) and (c) in figure 26(*a*) for the $m = 45$ roughness.

For the $m = 68$ roughness, the different data curves also correspond to measurements taken at different azimuthal locations. However, in this case, they were at two different pressure minima between different pairs of stationary cross-flow vortices. As a result there is more variation than with the $m = 45$ roughness that only considered one vortex pair. Again, linear least-squares-error fits were applied to the rapid increasing portion of the pressure data. These fell into two groups labelled (a) and (b) in figure 26(*b*). The pretransitional pressure baseline was determined to be $P_t/P_0 = 0.025$. Based on the intercept of the linear curves to the pressure baseline, the transition Reynolds number was estimated to be $Re_{x_{trans}} = 2.10 \times 10^6$ for group (a) and $Re_{x_{trans}} = 2.50 \times 10^6$ for group (b). The transition Reynolds number estimates based on the two methods for the patterned roughness cases are summarized in table 1.

The locations of the transition fronts for the baseline smooth tip and the $m = 45$ and 68 patterned roughness are shown in figure 21. These are based solely on the Preston

https://doi.org/10.1017/jfm.2012.579 Published online by Cambridge University Press

Roughness	$(Re_{x_{trans}} \times 10^6)_1$	$(Re_{x_{trans}} \times 10^6)_2$
$m = 45$	2.5	1.6–1.7
$m = 68$	3.5	2.1–2.5

TABLE 1. Transition Reynolds number locations based on method and roughness

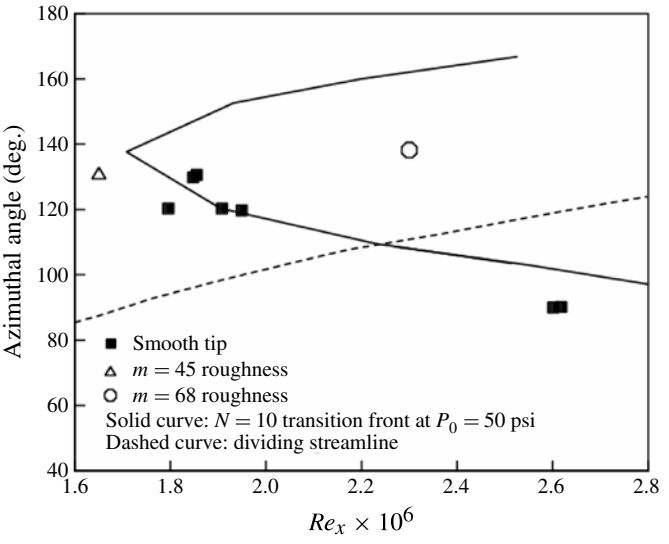


FIGURE 27. Transition locations based on a Preston tube approach for the baseline smooth tip, and the $m = 45$ and 68 patterned roughness.

tube approach. For the patterned roughness, the symbols represent the average values of Re_{trans} from table 1.

The filled square symbols in figure 21 correspond to the transition locations for the smooth tip. The solid curve corresponds to the transition front prediction for an N-factor of 10 and $P_0 = 50$ psi from Balakumar (2009). Although the stagnation pressure in the experiment is slightly lower than in the simulation, the agreement in the shape of the transition front is reasonably good.

The transition location for the $m = 45$ roughness is shown by the open triangle. This roughness was meant to be a controlled baseline. The transition location is indeed close to the $N = 10$ transition front that was representative of the smooth tip condition. The transition location for the $m = 68$ roughness is shown by the octagon symbol. The transition Reynolds number in this case is approximately 35 % higher than that of the uncontrolled baseline smooth tip and approximately 40 % higher than that of the controlled baseline $m = 45$ roughness.

4. Results: plasma distributed roughness

The results in this section document the receptivity of the stationary cross-flow mode to the plasma actuator array that was designed to replicate the passive patterned roughness. The same critical and subcritical azimuthal wavenumbers, $m = 45$ and 68, were investigated. The results focus on azimuthal profiles of the total pressure that

https://doi.org/10.1017/jfm.2012.579 Published online by Cambridge University Press

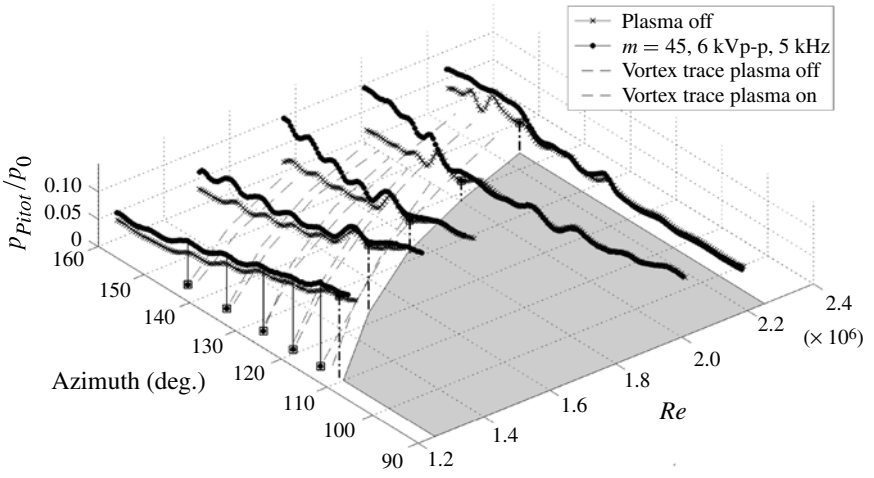


FIGURE 28. Azimuthal variation in mean pressure in the boundary layer at different axial locations for the critical wavenumber $m = 45$ plasma roughness operating (filled-circle symbols) and not operating (x symbols). Here $P_0 = 172.4$ kPa (25 psi).

document the mean flow distortion produced by the stationary cross-flow vortices. As with the passive roughness, these measurements provide an indication of the presence and characteristics of the stationary cross-flow modes in the boundary layer for the different 'plasma roughness' initial conditions. For these measurements, the only stagnation pressure investigated was $P_0 = 172.4$ kPa (25 psi), which corresponds to $Re_x = 2.79 \times 10^6$. This was the lower of the two stagnation pressures used for the passive roughness. This was suitable since our objective was to demonstrate that the stationary cross-flow modes were receptive to the 'plasma roughness'. With similar receptivity, we expected that transition control benefits would be comparable to the passive roughness.

Figures 28 and 29 show the azimuthal variation of the total pressure at a fixed height in the boundary layer at different axial locations for the $m = 45$ and $m = 68$ plasma roughness cone tips, respectively. The curves with the x-symbols correspond to the condition with the plasma roughness not operating. This is intended to document any passive effect of the electrode array. The curves with the filled-circle symbols correspond to when the plasma roughness is active. The periodic maxima of the azimuthal pressure distributions at each axial location are connected to indicate the trajectories of the stationary cross-flow vortices with the plasma off and on conditions. The shaded region denotes the 'dividing line' that was determined with the passive roughness and below which, any patterned roughness at the cone tip location is not sensed by the flow.

The azimuthal variation of the total pressure for the two plasma roughness cases clearly documents that the amplitude of the periodic total pressure fluctuations is always larger with the plasma actuator array operating than with it not operating. In addition, the pressure fluctuation amplitudes for the plasma roughness operating and not-operating conditions converge nearly precisely at the 'dividing line' boundary. This is most clearly evident with the larger azimuthal extent of the measurements for the $m = 68$ case in figure 29, and provides further evidence of the location of the dividing line.

https://doi.org/10.1017/jfm.2012.579 Published online by Cambridge University Press

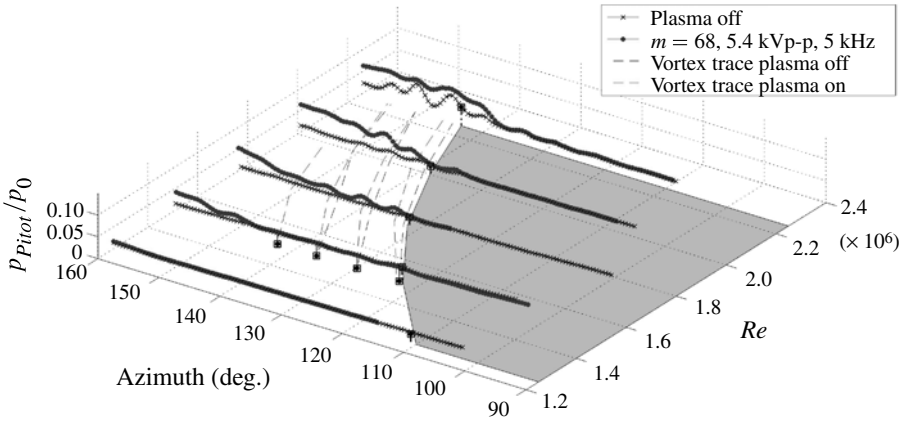


FIGURE 29. Azimuthal variation in mean pressure in the boundary layer at different axial locations for the subcritical wavenumber $m = 68$ plasma roughness operating (filled-circle symbols) and not operating (x symbols). Here $P_0 = 172.4$ kPa (25 psi).

Although the predominant wavenumber of the azimuthal pressure fluctuations appears to be close with the plasma roughness off and on, the trajectories of the maxima shown as the dashed curves, clearly indicate a difference. This is evident for both the $m = 45$ and 68 plasma roughness.

As a final point, we note that the amplitudes of the stationary cross-flow modes below the 'dividing streamline', were notably lower with the plasma roughness tip cases than with the 'smooth' tip. We believe the reason for this is that much greater care was taken in the machining of the Macor tip for the plasma actuator array to provide an extremely smooth surface (equivalent to 3200 grit as noted previously) so that the copper electrodes could be deposited onto the surface. We expect that as a result of the differences in the materials and fabrication, that the 'smooth' tip was not as smooth as the Macor plasma tips. As a result, the initial amplitudes of the stationary cross-flow modes outside the region of control of the plasma actuator array, was lower than with the 'smooth' tips, with the result being noticeably lower stationary cross-flow mode amplitudes downstream.

A further indication of the receptivity of the stationary cross-flow mode to the plasma roughness is the repeatability of the features in the azimuthal distribution of the total pressure in the boundary layer that is indicative of the mean flow distortion. As with the passive roughness, this involved successive measurements in which the wind tunnel was stopped and restarted. The results for the subcritical $m = 68$ 'plasma roughness' that were measured at an axial location where $Re_x = 2.0 \times 10^6$, are shown in figure 30. At the larger azimuthal angles that are above the 'dividing line' (unshaded region), the amplitude and locations of the pressure peaks and valleys were exactly repeatable. Below the 'dividing line' (shaded region) where the mean flow does not encounter roughness at the cone tip, the azimuthal pressure distribution was not repeatable. The strong contrast between the two regions confirms that the stationary cross-flow modes were receptive to the 'plasma roughness'.

Finally the effect of the AC voltage amplitude and frequency supplied to the 'plasma roughness' was investigated. The results for the subcritical $m = 68$ 'plasma roughness' are shown in figure 31. This again involved measurements of the azimuthal distribution of the total pressure in the boundary layer at an axial location where $Re_x = 2.0 \times 10^6$.

https://doi.org/10.1017/jfm.2012.579 Published online by Cambridge University Press

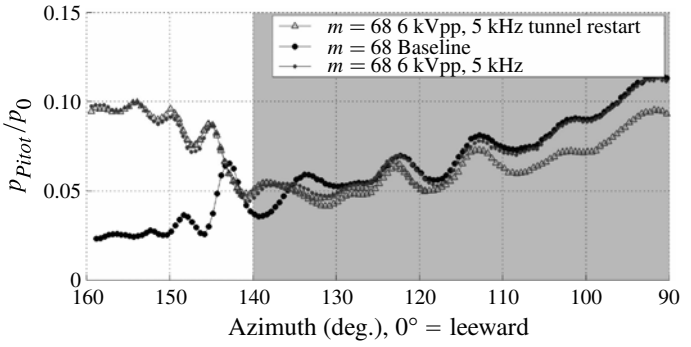


FIGURE 30. Repeated azimuthal profiles of the total pressure at a fixed height (approximately 0.2 mm) in the boundary layer for the $m = 68$ 'plasma roughness' cone tip while operating and while not operating ($P_0 = 172.4$ kPa). Here $Re_x = 2 \times 10^6$.

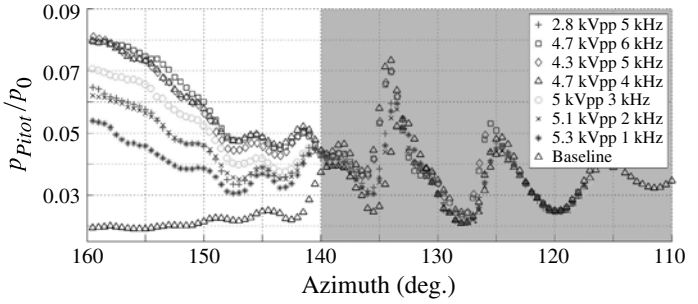


FIGURE 31. Repeated azimuthal profiles of the total pressure at a fixed height (0.2 mm) in the boundary layer for the $m = 68$ 'plasma roughness' cone tip at different AC voltage and frequency combinations. Here $Re_x = 2 \times 10^6$ or $x = 20.3$ cm.

In one set of measurements, the AC amplitude to the 'plasma roughness' was kept approximately constant, near 5 kV_{p-p}, and the AC frequency was varied between 1 and 6 kHz. The dielectric barrier discharge (DBD) body force is known to scale linearly with the AC voltage frequency (Corke *et al.* 2010). Therefore, we expected that the effect of the plasma roughness should scale linearly with the AC voltage frequency as well. The results for AC frequencies from 1 to 3 kHz, supported this expectation, with the pressure curves shifting upward in linear proportion to the ratio of the AC frequencies. For the AC frequencies from 4 to 6 kHz, the amplitudes stopped increasing, but rather saturated. This amplitude saturation is most likely an indication that at these active forcing levels, the cross-flow instability had reached nonlinear amplitudes by this axial location.

In another set of measurements documented in figure 31, the AC voltage frequency was held fixed at 5 kHz, and the AC voltage was increased from 2.8 to 4.3 kV_{p-p}. For a change in AC voltage, the body force scales as V^m_{p-p} (Corke *et al.* 2010). The exponent, m, depends on the static pressure, P_s. In the experiment at Mach 3.5 with $P_0 = 172.4$ kPa, $P_s = 10$ kPa. At this static pressure, $m = 2.4$ (Valerioti 2010). Based on this, a change in the AC voltage from 2.8 to 4.3 kV_{p-p} would result in an approximately factor of four increase in the 'plasma roughness' body force. This

https://doi.org/10.1017/jfm.2012.579 Published online by Cambridge University Press

is approximately 2.5 times the change in the body force caused by changing the AC voltage frequency from 1 to 6 kHz.

Examining the result of changing the AC voltage amplitude in figure 31 reveals that the pressure distribution at 2.8 kV_{p-p} and 5 kHz, fell nearly perfectly on the data at 5.1 kV_{p-p} and 2 kHz. This substantiates both the AC voltage scaling and receptivity repeatability of the 'plasma roughness'. At the higher AC voltage, the pressure distribution fell on the data at the higher AC frequencies, where the response was nonlinearly saturated.

The loss of the peak–valley structure in the pressure distributions at the higher azimuthal angles, $\theta \geqslant 150°$, suggests that based on the P_{rms} criterion we used previously, the boundary layer is transitional. This is consistent with the asymptotic response of the stationary cross-flow amplitude with the plasma roughness input amplitude.

An interesting result with the $m = 68$ plasma roughness is the appearance of a low wavenumber variation near $m = 35$, in the azimuthal pressure profiles in the region below the dividing line. This is quite evident in the shaded region in figure 31. We can only speculate on its source. According to the linear stability analysis in figure 5, $25 \leqslant m \leqslant 45$ are amplified for axial rays at lower azimuthal angles, $90° \leqslant \theta \leqslant 120°$, below the dividing line. At $\theta = 120°$, $m = 35$ is relatively highly amplified.

It is also interesting that the spectral analysis of the surface flow visualization for the $m = 68$ passive roughness also indicated significant energy at $m \simeq 35$. Therefore, although we do not know its origin, it is consistent between the $m = 68$ dimples and the $m = 68$ plasma roughnesses.

5. Conclusions

Experiments in the three-dimensional boundary layer on a right-circular cone at an angle of attack demonstrated the receptivity of stationary cross-flow modes to passive and active patterned roughness at Mach 3.5. The passive roughness consisted of micrometre-sized indentations (dimples) that were located near the cone tip, just upstream of the first neutral growth branch of stationary cross-flow modes, based on linear stability theory. The roughness dimples encircled the cone tip with a uniform spacing that defined the azimuthal wavenumber of the roughness. Two azimuthal wavenumbers of roughness were investigated: one that was in the band of the initially amplified wavenumbers of stationary cross-flow modes; the other that was at a 1.5 times higher wavenumber. The lower (critical) wavenumber patterned roughness was intended to represent a controlled baseline that would favour a single wavenumber stationary cross-flow mode. The higher (subcritical) wavenumber patterned roughness was designed to suppress the growth of initially amplified stationary cross-flow modes and thereby increase the transition Reynolds number, in a scenario first documented by Saric *et al.* (1998*b*). A smooth cone tip representing an uncontrolled baseline was used to confirm linear theory predictions and to provide contrast to the critical wavenumber roughness case.

The results confirmed that the stationary cross-flow modes were receptive to the passive patterned roughness. Repeated experiments with the passive roughness produced an identical response in the characteristics of the stationary cross-flow vortices that was not present with the uncontrolled smooth-tip baseline.

Transition front measurements using the Preston tube approach indicated that the transition Reynolds number had increased by 35 % with the subcritical wavenumber

https://doi.org/10.1017/jfm.2012.579 Published online by Cambridge University Press

roughness compared with the baseline smooth tip cone and by 40 % compared with the critical wavenumber roughness.

The active patterned roughness consisted of an azimuthal array of micrometre-sized DBD plasma actuators. The plasma actuators were designed to mimic surface roughness by producing pairs of counter-rotating streamwise vortices. The azimuthal wavenumber of these was the same as with the critical and subcritical passive roughness. The streamwise location on the cone tip was also the same as with the passive roughness.

The stationary cross-flow modes were found to be as receptive to the plasma actuator array (plasma roughness) as it was to the passive roughness. An input power range to the plasma actuator array that produced a linear response in the stationary cross-flow modes was established. The repeatability of the stationary cross-flow modes was as good as with the passive roughness.

Although not attempted, based on the similarities in the response of the stationary cross-flow modes, we expect that the subcritical wavenumber plasma roughness would produce a similar transition delay as the passive roughness. The advantage of the plasma roughness is that it can be designed to produce a range of azimuthal wavenumbers that can adapt to changing conditions that dictate the cross-flow stability characteristics.

Acknowledgements

The authors are indebted to S. Wilkinson, P. Balakumar, L. Owens and G. Beeler at the NASA Langley Research Center for their help in this research. The research was supported under the NASA NRA/Research Opportunities in Aeronautics Program Cooperative Agreement NNX08AB22A.

REFERENCES

BALAKUMAR, P. 2009 Stability of supersonic boundary layers on a cone at an angle of attack. In *39th Fluid Dynamics Conference and Exhibit*, 22–25 June 2009, San Antonio, TX, paper AIAA-2009-3555.

BECKWITH, I. E. 1974 Development of a high Reynolds number quiet tunnel for transition research. *AIAA J.* **13** (3), 300–306.

BIPPES, H. 1999 Basic experiments on transition in three-dimensional boundary layers dominated by crossflow instability. *Prog. Aerosp.* **35**, 363–412.

BONFIGLI, G. & KLOKER, M. 2007 Secondary instability of crossflow vortices: validation of the stability theory by direct numerical simulation. *J. Fluid Mech.* **583**, 229–272.

CAVALIERI, D. 1995 On the experimental design for instability analysis on a cone at Mach 3.5 and 6 using corona discharge pertubation method. MS thesis, Illinois Institute of Technology, Chicago, IL.

CHERNORAY, V. G., DOVGAL, A. V., KOZLOV, V. V. & LOEFDAHL, L. 2005 Experiments on secondary instability of streamwise vortices in a swept-wing boundary layer. *J. Fluid Mech.* **534**, 295–325.

CORKE, T. C. 2001 Plasma actuator array development for cross-flow instability control. *Internal Report*, UND-1-01.

CORKE, T., CAVALIERI, D. & MATLIS, E. 2002 Boundary layer instability on sharp cone at Mach 3.5 with controlled input. *AIAA J.* **40** (5), 1015–1018.

CORKE, T. C., ENLOE, C. L. & WILKINSON, S. P. 2010 Dielectric barrier discharge plasma actuators for flow control. *Annu. Rev. Fluid Mech.* **42**, 505–529.

CORKE, T. C. & KNASIAK, K. F. 1998 Stationary travelling cross-flow mode interactions on a rotating disk. *J. Fluid Mech.* **355**, 285–315.

https://doi.org/10.1017/jfm.2012.579 Published online by Cambridge University Press

CORKE, T., MATLIS, E. & OTHMAN, H. 2007 Transition to turbulence in rotating-disk boundary layers – convective and absolute instabilities. *J. Engng Maths* **57**, 253–272.

DICRISITINA, V. 1970 Three-dimensional laminar boundary-layer transition on a sharp 8° cone at Mach 10. *AIAA J.* **8** (5), 852–856.

KEGERISE, M. A., OWENS, L. R. & KING, R. A. 2010 High-speed boundary-layer transition induced by an isolated roughness element. In *40th Fluid Dynamics Conference and Exhibit*, 28 June–1 July, *AIAA Paper* 2010-4999, Chicago, Illinois.

KING, R. A. 1992 Three-dimensional boundary-layer transition on a cone at Mach 3.5. *Exp. Fluids* **13**, 305–314.

MALIK, M. R. 1995 eMalik3d: an e^N code for three-dimensional flow over finite-swept wings. High Technology Report No. HTC-9502.

MATLIS, E. H. 2003 Controlled experiments on instabilities and transition to turbulence on a sharp cone at Mach 3.5. PhD thesis, University of Notre Dame, Notre Dame, IN.

MORKOVIN, M. V. 1990*a* On roughness-induced transition: facts, views and speculation. In *Instability and Transition*, vol. I. Springer.

MORKOVIN, M. V. 1990*b* Panel summary on roughness. In *Instability and Transition*, vol. I. Springer.

RADEZTSKY, R. H. Jr., REIBERT, M. S. & SARIC, W. S. 1999 Effect of isolated micron-sized roughness on transition in swept-wing flows. *AIAA J.* **37** (11), 1370–1377.

REED, H. L. & SARIC, W. S. 1989 Stability of three-dimensional boundary layers. *Annu. Rev. Fluid Mech.* **21**, 235–284.

REIBERT, M. S. 1996 Nonlinear stability, saturation, and transition in crossflow-dominated boundary layers. PhD thesis, Arizona State University.

RESHOTKO, E. 2008 Paths to taransition wall layers. Papers presented during the AVT-151 RTO AVT/VKI Lecture Series held at the von Kármán Institute, Rhode St. Gense, Belgium, 9–12 June.

SARIC, W. S., CARRILLO, R. B. & REIBERT, M. S. 1998*a* Nonlinear stability and transition in 3-D boundary layers. *Meccanica* **33**, 469–187.

SARIC, W. S. & REED, H. L. 2002 Supersonic laminar flow control on swept wings using distributed roughness. *AIAA Paper* 2002-0147.

SARIC, W. S. & REED, H. L. 2003 Crossflow instabilities-theory and technology. *AIAA Paper* 2003-0771.

SARIC, W. S., REED, H. L. & BANKS, D. W. 2004 Flight testing of laminar flow control in high-speed boundary layers. Paper presented at the RTO AVT Specialists' Meeting on 'Enhancement of NATO Military Flight Vehicle Performance by Managemenet of Interacting Boundary Layer Transition and Separation', held in Prague, Czech Republic, 4–7 October 2004, published in RTO-MP-AVT-111.

SARIC, W. S., REED, H. L. & KERSCHEN, E. J. 2002 Boundary-layer receptivity to freestream disturbances. *Annu. Rev. Fluid Mech.* **34**, 291–319.

SARIC, W. S., REED, H. L. & WHITE, E. B. 2003 Stability and transition of three-dimensional boundary layers. *Annu. Rev. Fluid Mech.* **35**, 413–440.

SARIC, W. S., RUBEN, C. C. & REIBERT, M. S. 1998*b* Leading-edge roughness as a transition control mechanism. *AIAA Paper* AIAA-98-0781.

SCHUELE, C.-Y. 2011 Control of stationary cross-flow modes in a Mach 3.5 boundary layer using passive and active roughness. PhD thesis, University of Notre Dame, Notre Dame, IN.

SEMIONOV, N. V. & KOSINOV, A. D. 2007 Method laminar-turbulent transition control of supersonic boundary layer on a swept wing. *Thermophys. Aeromech.* **14** (3), 337–341.

SEMIONOV, N. V., KOSINOV, A. D. & LEVCHENKO, V. YA. 2006 Experimental study of turbulence beginning and transition control in a supersonic boundary layer on swept wing. In Sixth IUTAM Symposium on Laminar Turbulent Transition (R. Govindarajan), pp. 355–361, Fluid Mechanics and Its Applications, Vol. 78, ISBN 978-1-4020-3459-6.

STETSON, K. F. 1980 Hypersonic boundary layer transition experiments. Air Force Wright Aeronautical Laboratories Technical Report AFWAL-TR-80-3062.

VALERIOTI, J. 2010 Pressure dependence of plasma actuated flow control. MS thesis, University of Notre Dame, Notre Dame, IN.

https://doi.org/10.1017/jfm.2012.579 Published online by Cambridge University Press

WASSERMAN, P. & KLOKER, M. 2002 Mechanisms and passive control of crossflow-vortex-induced transition in a three-dimensional boundary layer. *J. Fluid Mech.* **456**, 49–84.

WHITE, E. & SARIC, W. 2000 Application of variable leading-edge roughness for transition control on swept wings. In *AIAA Paper* 2000-0283.

WHITE, E. B. & SARIC, W. S. 2005 Secondary instability of crossflow vortices. *J. Fluid Mech.* **525**, 275–308.

WILKINSON, S. P., ANDERS, S. G., CHEN, F. J. & BECKWITH, I. E. 1992 Supersonic and hypersonic quiet tunnel technology at NASA langley. In *AIAA 17 Aerospace Ground Testing Conference, Nashville, TN*.

WOLF, S. W. D. & LAUB, J. A. 1997 NASA Ames Laminar Flow Supersonic WInd Tunnel (LFSWT) Tests of a 10° Cone at Mach 1.6. NASA Technical Memorandum NASA-TM 110438.

https://doi.org/10.1017/jfm.2012.579 Published online by Cambridge University Press